

Mapping the cold dust temperatures and masses of nearby KINGFISH galaxies with *Herschel*

M. Galametz,^{1*} R. C. Kennicutt,¹ M. Albrecht,² G. Aniano,³ L. Armus,⁴ F. Bertoldi,² D. Calzetti,⁵ A. F. Crocker,⁵ K. V. Croxall,⁶ D. A. Dale,⁷ J. Donovan Meyer,⁸ B. T. Draine,³ C. W. Engelbracht,⁹ J. L. Hinz,⁹ H. Roussel,¹⁰ R. A. Skibba,⁹ F. S. Tabatabaei,¹¹ F. Walter,¹¹ A. Weiss,¹² C. D. Wilson¹³ and M. G. Wolfire¹⁴

¹*Institute of Astronomy, University of Cambridge, Madingley Road, Cambridge CB3 0HA*

²*Argelander-Institut für Astronomie, Abteilung Radioastronomie, Auf dem Hügel, D-53121 Bonn, Germany*

³*Department of Astrophysical Sciences, Princeton University, Princeton, NJ 08544, USA*

⁴*Spitzer Science Center, California Institute of Technology, MC 314-6, Pasadena, CA 91125, USA*

⁵*Department of Astronomy, University of Massachusetts, Amherst, MA 01003, USA*

⁶*Department of Physics and Astronomy, University of Toledo, Toledo, OH 43606, USA*

⁷*Department of Physics and Astronomy, University of Wyoming, Laramie, WY 82071, USA*

⁸*Department of Physics and Astronomy, SUNY Stony Brook, Stony Brook, NY 11794-3800, USA*

⁹*Steward Observatory, University of Arizona, Tucson, AZ 85721, USA*

¹⁰*Institut d'Astrophysique de Paris, F-75014 Paris, France*

¹¹*Max-Planck-Institut für Astronomie, Königstuhl 17, D-69117 Heidelberg, Germany*

¹²*Max-Planck-Institut für Radioastronomie, Auf dem Hügel 69, D-53121 Bonn, Germany*

¹³*Department of Physics and Astronomy, McMaster University, Hamilton, Ontario L8S 4M1, Canada*

¹⁴*Department of Astronomy, University of Maryland, College Park, MD 20742, USA*

Accepted 2012 June 29. Received 2012 June 28; in original form 2012 May 8

ABSTRACT

Taking advantage of the unprecedented combination of sensitivity and angular resolution afforded by the *Herschel Space Observatory* at far-infrared and submillimetre wavelengths, we aim to characterize the physical properties of cold dust within nearby galaxies, as well as the associated uncertainties, namely the robustness of the parameters we derive using different modified blackbody models. For a pilot subsample of the KINGFISH (Key Insights on Nearby Galaxies: A Far-Infrared Survey with *Herschel*) key programme, we perform two-temperature fits of the *Spitzer* and *Herschel* photometric data (from 24 to 500 μm), with a warm and a cold component, both globally and in each resolution element. We compare the results obtained from different analysis strategies. At global scale, we observe a range of values of the modified blackbody fit parameters β_c (0.8–2.5) and T_c (19.1–25.1 K). We compute maps of our modelling parameters with β_c fixed or treated as a free parameter to test the robustness of the temperature and dust surface density maps we deduce. When the emissivity is fixed, we observe steeper temperature gradients as a function of radius than when it is allowed to vary. When the emissivity is fitted as a free parameter, barred galaxies tend to have uniform fitted emissivities. Gathering the parameters obtained in each resolution element in a T_c – β_c diagram underlines an anticorrelation between the two parameters. It remains difficult to assess whether the dominant effect is the physics of dust grains, noise, or mixing along the line of sight and in the beam. We finally observe in both cases that the dust column density peaks in central regions of galaxies and bar-ends (coinciding with molecular gas density enhancements usually found in these locations). We also quantify how the total dust mass varies with our assumptions about the emissivity index as well as the influence of the wavelength coverage

*E-mail: mgalamet@ast.cam.ac.uk

used in the fits. We show that modified blackbody fits using a shallow emissivity ($\beta < 2.0$) lead to significantly lower dust masses compared to the $\beta < 2.0$ case, with dust masses lower by up to 50 per cent if $\beta_c = 1.5$, for instance. The working resolution affects our total dust mass estimates: masses increase from global fits to spatially resolved fits.

Key words: dust, extinction – galaxies: ISM – submillimetre: galaxies.

1 INTRODUCTION

The interstellar medium (ISM) plays a key role in the star formation history of galaxies. While stars evolve and die, they re-inject dust and gas in the ISM which will then be processed to form a new generation of stars. Dust is formed in the envelopes of late-evolved stars and is transformed in supernova shock waves or stellar winds by violent processes such as destruction, vaporization, sputtering or erosion (Jones et al. 1994; Jones, Tielens & Hollenbach 1996; Serra Díaz-Cano & Jones 2008). The size of dust grains also increases through processes like accretion or coagulation accretion (Dominik & Tielens 1997; Stepnik et al. 2003; Dominik & Dullemond 2008; Hirashita & Omukai 2009). They participate in the gas thermal balance and screen parts of the ISM through the absorption of starlight and subsequent emission of infrared (IR) photons.

Dust grains contribute to the chemistry of the ISM. Molecular hydrogen predominantly forms on grains, and molecules can freeze out on grain surfaces and undergo additional transformation (Hasegawa & Herbst 1993; Vidali et al. 2004; Cazaux et al. 2005). Atomic and molecular gas is commonly traced by H I and CO observations. CO can be a poor tracer of molecular gas, especially in low-metallicity environments, due to the dependency of the CO to H₂ conversion factor on density and metallicity (Wilson 1995; Taylor, Kobulnicky & Skillman 1998; Israel 2000; Leroy et al. 2005; Wolfire, Hollenbach & McKee 2010). We know that dust and gas are closely tied in the ISM. This suggests that when used with H I and CO, dust can also serve as an additional tracer of gas.

It is crucial to yield an exhaustive inventory on the range and distribution of dust temperatures as well as the radiative heating sources of dust grains. *IRAS* data combined with ground-based observations (SCUBA on JCMT, for instance, observing at 450 and 850 μm) have first led to the detection of the cool phases of dust in nearby galaxies (Dunne et al. 2000; Dunne & Eales 2001; James et al. 2002). The *Infrared Space Observatory* and the *Spitzer Space Telescope* (with a better sensitivity) then enabled us to resolve in detail the warm and cool dust reservoirs and more accurately model the spectral energy distribution (SED) of nearby objects up to 160 μm (Draine et al. 2007).

Several issues still have to be investigated. Numerous studies thus highlighted the necessity of observing galaxies longwards of 160 μm at high resolution to properly sample the submillimetre (submm) regime of these SEDs and better characterize the total temperature range and dust masses (e.g. Gordon et al. 2010). Moreover, IR emission is known to be a good tracer of the embedded star formation in galaxies (Kennicutt 1998; Calzetti 2007; Calzetti et al. 2010). Nevertheless, the amount of IR emission not directly linked with the ongoing star formation is still poorly quantified. To address this issue, we need to understand the heating sources of the different grain populations: dust heating by the young stellar populations in H II and photodissociation regions (PDRs) and ultraviolet photons escaping from those regions or old stellar populations.

The *Herschel Space Observatory* (Pilbratt et al. 2010) is currently observing the far-IR/submm wavelength range to probe the coldest

phases of dust that were poorly unexplored. Its onboard photometers PACS (from 70 to 160 μm) and SPIRE (from 250 to 500 μm) enable the imaging of nearby galaxies at a resolution and sensitivity never reached to date by a space telescope. The *Planck* satellite, launched by the same rocket, performs an all-sky survey at nine wavelengths between 350 μm and 1 cm, complementing *Herschel* coverage, at a lower resolution. Ade et al. (2011a) studies have suggested that some nearby galaxies are both luminous and cool (presence of dust with $T < 20$ K), with properties comparable to those of galaxies observed with *Herschel* at higher redshifts (Rowan-Robinson et al. 2010; Magnelli et al. 2012). Using *Herschel* observations, Engelbracht et al. (2010) compute separate SEDs for the centre and discs of nearby galaxies and find that the cool dust is on average 15 per cent hotter in the centre than in the disc and correlate this effect with morphological type and bar strength. Using a radial approach, Pohlen et al. (2010) show that SPIRE surface brightness ratios – used as a proxy for cold dust temperatures – seem to decrease with radius in spirals, and conclude that dust in the outer regions is colder than in the centre of the galaxies. Skibba et al. (2011) also investigate the relation between dust heating sources and the star formation activity with metallicity and the morphological types of their galaxies. On a more resolved scale, Bendo et al. (2012) derive PACS and SPIRE ratio maps of spiral galaxies. They find that those ratios seem to be preferentially correlated with the global starlight, including evolved stars, rather with emission from star-forming regions, results consistent with those obtained by Boquien et al. (2011) for the spiral Local Group galaxy M33 or by Auld et al. (2012) for extragalactic dust clouds of Centaurus A, among others. This supports the idea of a different source of heating for the cold (15–30 K) dust from that of the warm dust. Using *Herschel* observations of the dwarf irregular galaxy NGC 6822, Galametz et al. (2010) show, in contrast, that SPIRE surface brightness ratios are strongly correlated with the 24 μm surface brightness, a commonly used tracer of the star formation activity. This might indicate that star-forming regions are non-negligible heating sources of cold dust in that object and suggest that the source of dust heating probably differs with the environment and varies from normal spirals to low-metallicity starbursts.

Observations of galaxies with *Herschel* and from the ground have also suggested that the properties of cold dust grains could differ from those often used in SED models such as blackbody modified with an emissivity law index $\beta = 2$ or use of graphite grains to model carbon dust. In metal-poor objects in particular, using graphite grains can lead to unphysical gas-to-dust mass ratios compared to those expected from the metallicity of the galaxy (Galametz et al. 2010; Meixner et al. 2010). Moreover, observations of dwarf galaxies in submm often lead to the detection of excess emission compared to extrapolations from *Spitzer*-based fits (Galliano et al. 2003, 2005; Dumke, Krause & Wielebinski 2004; Bendo et al. 2006; Marleau et al. 2006; Galametz et al. 2009; Bot et al. 2010; O’Halloran et al. 2010). The origin of this excess is still an open issue and several explanations have been investigated so far: variations of the emissivity of the dust grains with temperature, ‘spinning

dust' emission, cold dust, etc. Many investigations still need to be carried out to disentangle between those different hypotheses.

We have obtained photometric *Herschel*/PACS (70–160 μm) and *Herschel*/SPIRE (250–500 μm) observations of nearby galaxies as part of the open time key programme KINGFISH (Key Insights on Nearby Galaxies: A Far-Infrared Survey with *Herschel*, Kennicutt et al. 2011). The KINGFISH sample comprises 61 galaxies probing a wide range of galaxy types (from elliptical to irregular galaxies), metallicity [$7.3 \leq 12 + \log(\text{O}/\text{H}) \leq 9.3$] and star-forming activity ($10^{-3} \leq \text{SFR} \leq 7 M_{\odot} \text{ yr}^{-1}$). The KINGFISH galaxies are located between 3 and 31 Mpc, leading to ISM resolution elements of 0.5–5.4 kpc at the SPIRE 500 μm resolution (36 arcsec). We refer to Kennicutt et al. (2011) for a detailed description of the sample and the observation strategy.

We aim to benefit from the good coverage and resolution of *Herschel* to sample the complete thermal dust emission spectrum and probe the spatially resolved properties of the cold dust grain population. We refer to the work of Aniano et al. (2012, hereafter A12a) and Aniano et al. (in preparation, hereafter A12b, full KINGFISH sample) for an analysis of other dust properties (polycyclic aromatic hydrocarbon contribution to the total dust mass, distribution of the starlight intensity, dust mass surface density, among others) in the KINGFISH sample using the Draine & Li (2007, hereafter DL07) dust models. The two studies are complementary. The latter particularly focuses on investigating the distribution of cold dust temperatures and dust mass surface densities in our objects. The SED model applied in this work [two-modified-blackbody (two-MBB) fit] allows for variations in the emissivity index of the dust grains and enables us to test the robustness of applying different assumptions of emissivity index to our extragalactic objects and quantify how this affects the temperatures and masses derived.

This paper is structured as follows. In Section 2, we describe the *Herschel* observations and the convolution techniques we apply to degrade images to the lowest resolution (that of SPIRE 500 μm). In Section 3, we discuss the integrated properties of the cold dust (temperature and emissivity). We also study how uncertainties in the flux measurements can lead to degeneracies between parameters. In Section 4, we produce maps of the dust properties of our galaxies and discuss the choice of a fixed or free emissivity parameter on the temperature and emissivity maps obtained. We also study the distribution of the dust mass surface densities in our objects. We finally analyse how the total dust mass depends on the type of

MBB model we apply, the wavelength coverage and the working resolution.

2 OBSERVATIONS AND DATA PROCESSING

2.1 The sample

The data taken with the *Herschel Space Telescope* now enable us to properly constrain the cold dust properties in nearby galaxies. In this paper, we focus our study on 11 galaxies, nine spirals and two lenticulars (NGC 1291 and 1316) observed as part of the *Herschel* open time key programme KINGFISH. Those galaxies were primarily selected because they have also been mapped at 870 μm with the LABOCA instrument located on APEX in Chile, data that will be analysed in a second paper in this series. Our galaxies (i) are observable from APEX ($\delta_{\text{o}} < +21^{\circ}$); (ii) are large enough to use the LABOCA mapping mode (the field of view of the complete array is 11.4 arcmin); (iii) have diffuse emission bright enough to be detected with LABOCA. Our sample is thus biased towards relatively high surface brightness normal spirals. Albrecht et al. (in preparation) describe the LABOCA observations and data reduction. We will combine LABOCA data with the results obtained in this paper to investigate possible 870 μm submm excess in our objects (Galamez et al., in preparation). The properties of our sample are summarized in Table 1. Morphologies and sizes as well as references and methods used to derive distances, and the total IR luminosity (L_{TIR}) are detailed in Kennicutt et al. (2011). The SFRs are derived using a combination of $\text{H}\alpha$ and 24 μm integrated luminosities taken from Calzetti et al. (2010). Two values are given for the oxygen abundance: one from the empirical calibration of Pilyugin & Thuan (2005, hereafter PT) and the other from the calibration of Kobulnicky & Kewley (2004, hereafter KK) as discussed in detail in Moustakas et al. (2010). The sample covers different morphologies and a wide range of bar strengths. It contains isolated targets as well as galaxies with disturbed outskirts resulting from past interactions, such as NGC 3627. It also contains mergers such as NGC 1316 (Fornax A), an early-type radio galaxy that could be interacting with NGC 1317, also detected in our *Herschel* field of view. NGC 1316 possesses a core–jet lobe structure (Ekers et al. 1983) and a low-luminosity X-ray active galactic nucleus (AGN) (Kim & Fabiano 2003). We discuss how this could affect our results later in the paper. The star formation rate (SFR) of our sample ranges from

Table 1. Galaxy data.

Galaxy	Optical morphology	α_0 (J2000)	δ_0 (J2000)	Major diameter (arcmin)	Minor diameter (arcmin)	Distance (Mpc)	12 + log(O/H) (PT)	12 + log(O/H) (KK)	SFR ($M_{\odot} \text{ yr}^{-1}$)	L_{TIR} ($\times 10^9 L_{\odot}$)
(1)	(2)	(3)	(4)	(5)	(6)	(7)	(8)	(9)	(10)	
NGC 337	SBd	00 ^h 59 ^m 50 ^s .7	−07° 34′ 44″	2.9	1.8	19.3	8.18	8.84	1.30	12.0
NGC 628	SAC	01 ^h 36 ^m 41 ^s .8	15° 47′ 17″	10.5	9.5	7.2	8.35	9.02	0.68	8.0
NGC 1097	SBb	02 ^h 46 ^m 18 ^s .0	−30° 16′ 42″	9.3	6.3	14.2	8.47	9.09	4.17	45.0
NGC 1291	SB0/a	03 ^h 17 ^m 19 ^s .1	−41° 06′ 32″	9.8	8.1	10.4	8.52	9.20	0.35	3.5
NGC 1316	SAB0	03 ^h 22 ^m 41 ^s .2	−37° 12′ 10″	12.0	8.5	21.0	8.77	9.52	–	8.0
NGC 1512	SBab	04 ^h 03 ^m 55 ^s .0	−43° 20′ 44″	8.9	5.6	11.6	8.56	9.11	0.36	3.8
NGC 3351	SBb	10 ^h 43 ^m 57 ^s .5	11° 42′ 19″	7.4	5.0	9.3	8.60	9.19	0.58	8.1
NGC 3621	SAd	11 ^h 18 ^m 18 ^s .3	−32° 48′ 55″	12.3	7.1	6.5	8.27	8.80	0.51	7.9
NGC 3627	SABb	11 ^h 20 ^m 13 ^s .4	12° 59′ 27″	9.1	4.2	9.4	8.34	8.99	1.7	28.0
NGC 4826	SAab	12 ^h 56 ^m 42 ^s .8	21° 40′ 50″	10.0	5.4	5.3	8.54	9.20	0.26	4.2
NGC 7793	SAd	23 ^h 57 ^m 50 ^s .4	−32° 35′ 30″	9.3	6.3	3.9	8.31	8.88	0.26	2.3

Columns: (1) – galaxy name; (2) – morphological type; (3) – right ascension (J2000.0); (4) – Dec. (J2000.0); (5) – approximate major diameter in arcminutes; (6) – approximate minor diameter in arcminutes; (7) – distance in megaparsecs; (8) – mean disc oxygen abundance from Moustakas et al. (2010); (9) – SFR in solar masses per year from table 1 of Calzetti et al. (2010); (10) – total IR luminosities in 3–1100 μm in units of 10^9 solar from Kennicutt et al. (2011).

0.3 to $8 M_{\odot} \text{ yr}^{-1}$ and the L_{TIR} covers an order of magnitude, from 2.3×10^9 to $4.5 \times 10^{10} L_{\odot}$. Our sample thus spans a wide range of environments and physical conditions to which dust is exposed. One of them, the barred galaxy NGC 1097, was observed and studied during the science demonstration phase of *Herschel*. It hosts a prominent starbursting ring with a radius of ~ 900 pc (Hummel, van der Hulst & Keel 1987). We refer to Sandstrom et al. (2010) and Beirão et al. (2010) for PACS photometric and spectroscopic studies of this circumnuclear ring. We also refer to Hinz et al. (2012) for a radial study of temperatures in NGC 1291, another galaxy of this sample. We benefit from the good spatial resolution of *Herschel* to resolve with SPIRE $500 \mu\text{m}$ (FWHM = 36 arcsec, where FWHM stands for full width at half-maximum) structures of ~ 700 pc for the closest galaxy of our sample NGC 7793 and ~ 4 kpc for the farthest galaxy NGC 1316. Three-colour images (24/100/250 μm) of the galaxies are provided in Fig. 1.

2.2 The *Herschel* observations

The KINGFISH programme observed their 61 nearby targets with the PACS and SPIRE instruments between 2009 December and 2011 June. A description of the data processing steps is given in Engelbracht et al. (2010), Sandstrom et al. (2010) and the KINGFISH overview paper of Kennicutt et al. (2011). A few details are summarized in the next sections.

2.2.1 PACS observations

The PACS photometer observes at 70, 100 and 160 μm with FWHM of 5.2, 7.7 and 12 arcsec, respectively (Poglitsch et al. 2010). Observations of KINGFISH galaxies with this instrument were obtained with 15-arcmin-long cross-scans (perpendicular scans) with a medium scan speed of 20 arcsec s^{-1} . PACS calibration uncertainties are ~ 5 per cent according to Version 4 of the PACS Observers' Manual.¹ The data reduction is performed from raw data to Level 1 data with the Version 5 of HIPE (Herschel Interactive Processing Environment) using the standard procedure with additional second-level deglitching steps. We use the SCANAMORPHOS technique to process the data from Level 1. SCANAMORPHOS is an IDL software which subtracts the brightness drifts caused by the low-frequency noise using the redundancy built in the observations. We refer to Roussel (in preparation) for a complete description of the software. PACS data emerge from the pipeline with a pixel size of 1.4, 1.7 and 2.85 arcsec at 70, 100 and 160 μm , respectively. We applied the needed correction factors to obtain the latest version (Version 6) of responsivity calibration. The root-mean-square (rms) noise levels are 0.14–0.18, 0.24–0.35 and 0.74–1.9 mJy arcsec $^{-2}$ at 70, 100 and 160 μm , respectively, for our subsample. The SCANAMORPHOS pipeline aims to preserve low surface brightness diffuse emission. Nevertheless, the PACS instrument is less sensitive than the MIPS instrument to low surface brightness emission. Our analysis of the resolved properties of our objects will be restricted to pixels for which we have a 3σ detection in all the bands.

2.2.2 SPIRE observations

The SPIRE instrument produces maps at 250, 350 and 500 μm with FWHM of 18, 25 and 36 arcsec, respectively (Griffin et al. 2010). Observations of KINGFISH galaxies with this instrument

were obtained in scan mode. The data reduction was performed from raw data with the Version 5 of HIPE. Details on the data reduction are given in the KINGFISH Data Products Delivery Users' Guide.² The SPIRE maps were built with a nearest neighbour projection on sky and averaging of the time-ordered data. SPIRE maps emerge from the pipeline with a pixel size of 6, 10 and 14 arcsec at 250, 350 and 500 μm , respectively. We use the SPIRE beam areas quoted in the SPIRE Observers' Manual, namely 423, 751 and 1587 arcsec 2 at 250, 350 and 500 μm , respectively, with ~ 1 per cent uncertainty. The rms noise levels are 0.5–0.75, 0.24–0.34 and 0.14–0.21 MJy sr^{-1} at 250, 350 and 500 μm , respectively, for our subsample. Calibration uncertainties are estimated to be ~ 7 per cent for the three wavebands.³

2.3 Background galaxies and sky subtraction

The background galaxies subtraction and sky subtraction steps are similar to those applied in Dale et al. (2012, hereafter D12) to derive the global photometry for the KINGFISH sample. We identify the bright background galaxies that could contaminate the photometry and 'remove' them by replacing the data with random values with similar noise characteristics. The removal of these background objects does not significantly affect the total flux estimates (< 1 per cent). The companion of NGC 1316 (NGC 1317) is also removed from the *Herschel* fields of view to avoid strong contamination in the chosen photometric aperture. A global sky subtraction is already applied on the PACS/SPIRE maps during the reduction process. However, this value was estimated on the entire map. We determine a refined local sky using apertures randomly distributed in the background. We choose the total 'sky' area to be greater than the area we choose to perform the photometry (see Table 2). We do not expect the Galactic cirrus to contaminate any of the galaxies of our sample. Indeed, the lowest Galactic latitude for the sample is $+26^\circ$ for NGC 3621.

2.4 Convolution to lower resolution maps

To compare the fluxes at different wavelengths, we need to convolve every observation to a common resolution. We refer to Aniano et al. (2011) for details on how to construct convolution kernels between *Spitzer* and *Herschel* bands. The main steps are similar to the technique described in Gordon et al. (2008). We review the basic steps here.

In-flight point spread functions (PSFs) are available for *Herschel*. An ideal convolution kernel $K(x, y)$ which transforms an original PSF (PSF $_0$) to a lower resolution final PSF (PSF $_f$) is defined as

$$K(x, y) = \text{FT}^{-1} \left[\frac{\text{FT}[\text{PSF}_f(x, y)]}{\text{FT}[\text{PSF}_0(x, y)]} \right]. \quad (1)$$

To attenuate the high-frequency noise in the original PSF, a filter is first applied to $\text{FT}[\text{PSF}_0(x, y)]$:

$$\text{Filter}(\omega) = \begin{cases} 1 & \text{for } \omega \leq \omega_{\text{low}} \\ \frac{1}{2} \left[1 + \cos \left(\pi \times \frac{\omega - \omega_{\text{low}}}{\omega_{\text{high}} - \omega_{\text{low}}} \right) \right] & \text{for } \omega_{\text{low}} \leq \omega \leq \omega_{\text{high}} \\ 0 & \text{for } \omega_{\text{high}} \leq \omega, \end{cases} \quad (2)$$

¹ http://herschel.esac.esa.int/Docs/PACS/html/pacs_om.html

² <http://herschel.esac.esa.int/UserReducedData.shtml>

³ http://herschel.esac.esa.int/Docs/SPIRE/html/spire_om.html

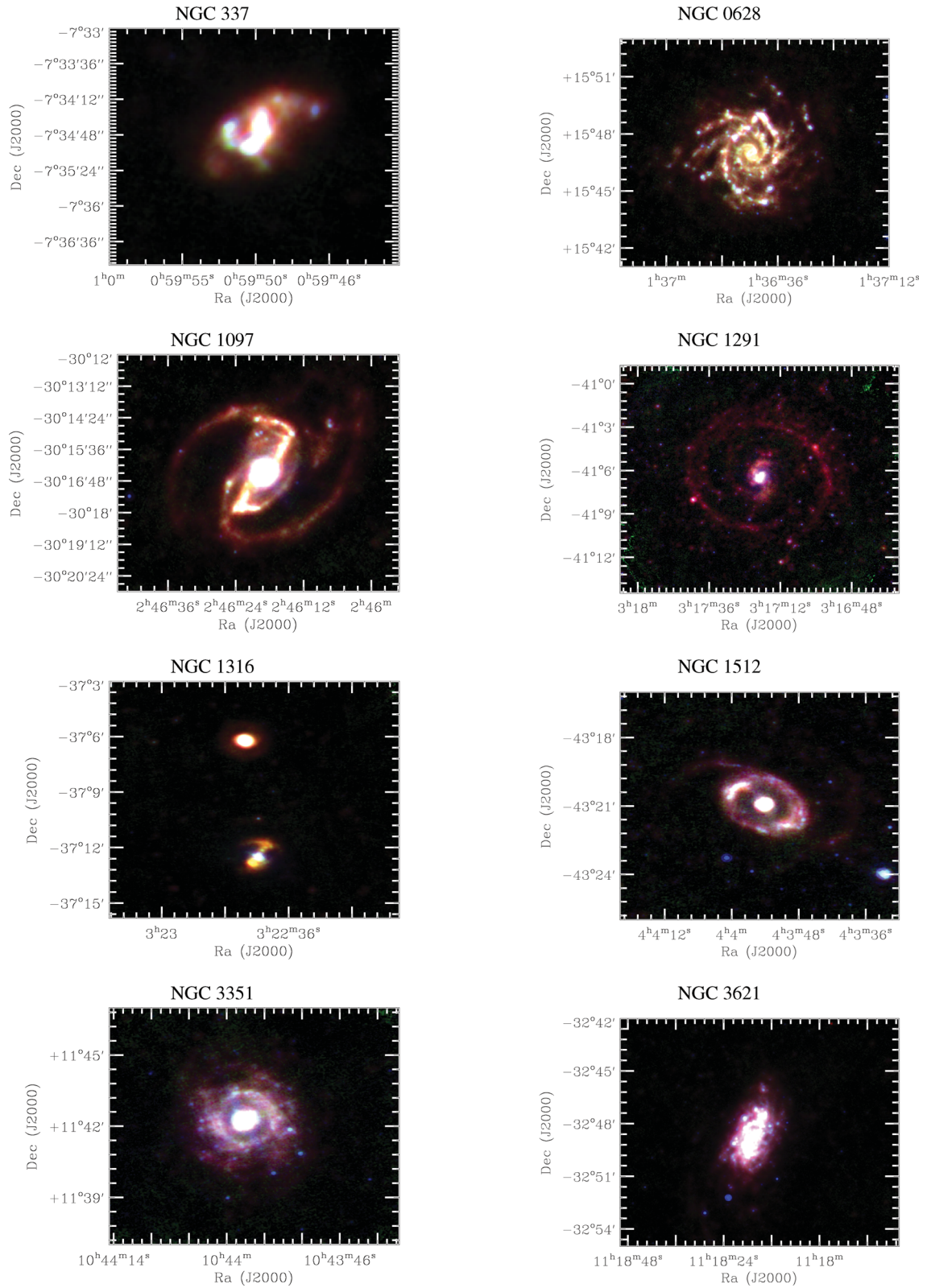
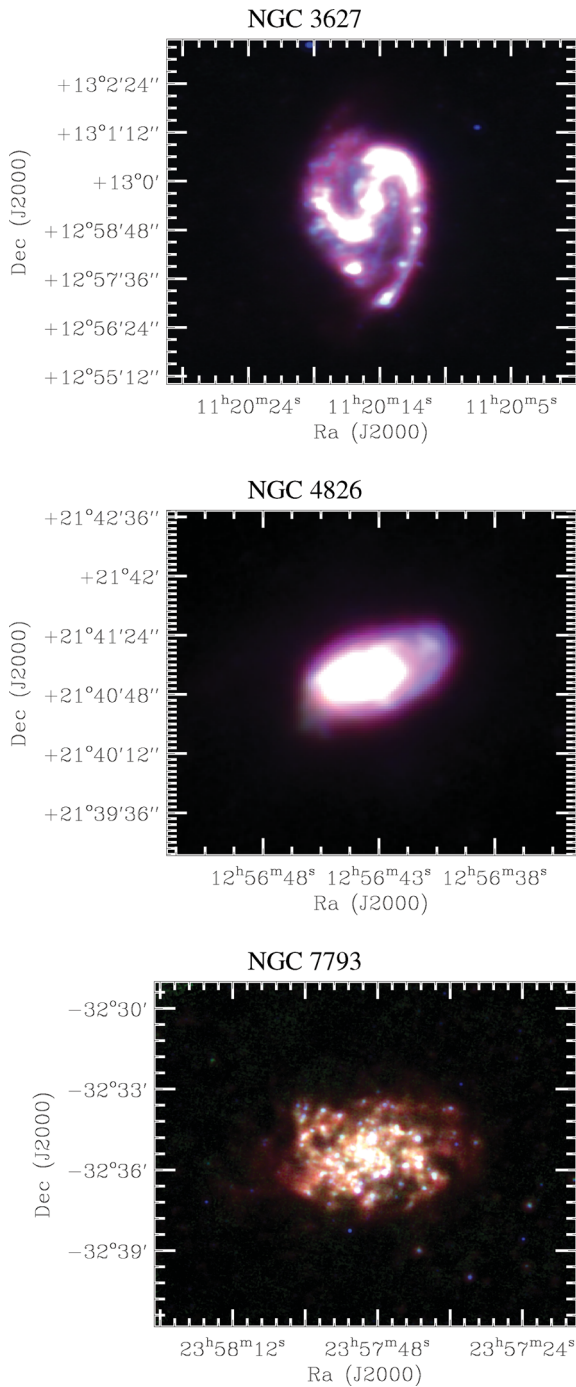


Figure 1. Three-colour images of the sample. In each panel, north is up and east is left. Blue: *Spitzer*/MIPS 24 μm . Green: *Herschel*/PACS 100 μm . Red: *Herschel*/SPIRE 250 μm . We note that NGC 1316 and its companion NGC 1317 are seen in our *Herschel* field of view. NGC 1317 is north of NGC 1316.

Figure 1 – *continued*

where ω_{high} is the cut-off spatial frequency and $\omega_{\text{low}} = 0.7\omega_{\text{high}}$. ω_{high} is appropriately chosen to reach a high accuracy but minimizes the noise linked with the process. The final kernels are circularized to produce rotationally symmetric kernels, thus independent of the relative orientation of the spacecraft.

We convolve MIPS, PACS and SPIRE images to the SPIRE 500 μm images using the previous kernels and the IDL procedure `conv_image`. We finally project the maps to a common sampling grid (that of the SPIRE 500 μm maps) with the IDL HASTROM procedure. Aniano et al. (2011) caution about convolutions from MIPS 160 μm to SPIRE 500 μm . The deconvolution of an image to higher resolution can indeed be risky if the image contains noise and arte-

facts. We compare the resolved PACS 160 μm flux densities (pixels about 3σ in the band) for the whole sample with the resolved MIPS 160 μm flux densities (maps convolved to the SPIRE 500 μm resolution). We find a very good agreement between the two values and therefore decide to use both in the modelling. As mentioned in A12a, among others, slight discrepancies can be observed between MIPS and PACS fluxes. We know, for instance, that the PACS instrument is less sensitive to diffuse emission than MIPS. Using both MIPS and PACS (at 70 and 160 μm) data enables us to be more careful and conservative in our modelling. The model will indeed try to find a compromise between the two values.

3 INTEGRATED PROPERTIES

3.1 Naming convention

The SED peak emission of nearby galaxies spans a relatively narrow range of dust temperatures, from ~ 15 to 40 K (Bendo et al. 2003; Dale et al. 2005; Stevens, Amure & Gear 2005; Boselli et al. 2010; D12). In this study, we decide to use an isothermal fit to describe the cold dust component and to call our parameter T_c the ‘cold dust temperature’. It is nevertheless important to keep in mind that the temperature distribution of the cold dust phase is more complex than a delta function, with a range of cold grain temperatures along the line of sight. The ‘cold dust temperatures’ derived in this paper (and in other studies using similar fitting procedures) should be considered in reality as an approximation of the cold temperature distribution in our galaxies. Moreover, an emissivity index is, by definition, the power-law index describing the variation of dust opacity with wavelength, so an intrinsic property of the grains. Calling our parameter β_c the ‘cold dust emissivity index’ is a commonly used expression. Our parameter β_c is more accurately the ‘effective emissivity index’, namely a power-law index resulting from the sum of different grain populations, each of them having their own intrinsic emissivity index. The effective and intrinsic emissivity indices are identical in the isothermal case.

3.2 The model

We first want to derive integrated dust properties of our sample to investigate the variations of the cold dust temperature and emissivity between objects. A combination of data from 24 to 500 μm provides a complete sampling of the warm and cold dust thermal emission of our galaxies from which global dust properties can be deduced. The submm data are, in particular, crucial to constrain the coldest phases of dust that could account for a large amount of the dust mass. They also enlighten us as to how the properties of cold dust vary from galaxy to galaxy.

We use the global PACS and SPIRE fluxes of KINGFISH galaxies derived by D12. Their elliptical apertures (Table 2) are similar to those used to perform the *Spitzer* photometry [for *Spitzer* Infrared Nearby Galaxies Survey (SINGS) in particular] and encompass the total emission of the galaxy at each wavelength. Global fluxes are measured on original resolution images. We complement the global SED coverage with data from *Spitzer*/MIPS and *IRAS*. We use the global flux densities of our galaxies for *Spitzer*/MIPS bands derived by Dale et al. (2007). We obtain the *IRAS* global flux densities at 25, 60 and 100 μm (accurate to ~ 20 per cent, when available) through the `SCANPI`⁴ tool (*IRAS* Scan Processing and Integration tool) and the

⁴ <http://scanpiops.ipac.caltech.edu:9000/applications/Scanpi/index.html>

Table 2. Global IRAS, MIPS, PACS and SPIRE flux densities (in units of Jy).

	NGC 337	NGC 628	NGC 1097	NGC 1291	NGC 1316	NGC 1512	NGC 3351	NGC 3621	NGC 3627	NGC 4826	NGC 7793
$2a^a$	253	879	758	884	864	1001	592	791	745	716	716
$2b^a$	194	808	612	836	583	928	441	555	486	427	526
α^a	140	90	130	90	50	83	11	160	167	114	98
MIPS 24 μm^b	0.7 ± 0.03	3.2 ± 0.1	6.6 ± 0.3	0.6 ± 0.02	0.4 ± 0.02	0.5 ± 0.02	2.6 ± 0.1	3.7 ± 0.2	7.4 ± 0.3	2.7 ± 0.2	2.1 ± 0.1
IRAS 25 μm^c	0.7 ± 0.1	2.9 ± 0.6	8.6 ± 1.7	0.5 ± 0.1	0.4 ± 0.09	0.5 ± 0.1	2.8 ± 0.6	4.2 ± 0.8	8.6 ± 1.7	2.9 ± 0.6	1.7 ± 0.3
IRAS 60 μm^c	9.4 ± 1.9	21.6 ± 4.3	54.4 ± 10.9	2.8 ± 0.6	3.3 ± 0.7	3.8 ± 0.8	19.7 ± 3.9	32.2 ± 6.4	66.3 ± 13.3	36.7 ± 7.3	18.1 ± 3.6
MIPS 70 μm^b	11.2 ± 0.8	33.9 ± 4.1	59.8 ± 4.7	5.3 ± 0.6	5.4 ± 0.4	6.8 ± 0.8	21.9 ± 2.7	50.2 ± 3.9	91.9 ± 7.0	52.9 ± 6.5	32.9 ± 4.0
PACS 70 μm^d	13.0 ± 0.7	36.7 ± 1.8	77.5 ± 3.9	5.3 ± 0.3	5.8 ± 0.3	8.0 ± 0.5	25.3 ± 1.3	49.5 ± 2.5	104 ± 5.0	54.7 ± 2.7	32.0 ± 1.6
IRAS 100 μm^c	20.2 ± 4.0	54.5 ± 10.9	115 ± 23.0	11.5 ± 2.3	9.2 ± 1.8	12.6 ± 2.5	41.1 ± 8.2	82.1 ± 16.4	137 ± 27.3	81.7 ± 16.3	54.1 ± 10.7
PACS 100 μm^d	19.5 ± 1.0	74.0 ± 3.7	116 ± 6.0	12.8 ± 0.7	9.3 ± 0.5	13.8 ± 0.7	46.1 ± 2.3	94.4 ± 4.7	179 ± 9.0	95.7 ± 4.8	65.8 ± 3.3
MIPS 160 μm^b	20.1 ± 2.4	112 ± 17	154 ± 19	26.3 ± 4.1	12.6 ± 1.8	19.6 ± 3.1	56.9 ± 8.9	139 ± 17	216 ± 28	85.8 ± 13	107 ± 17
PACS 160 μm^d	19.6 ± 1.0	116 ± 6.0	134 ± 7.0	20.3 ± 1.1	11.5 ± 0.6	18.7 ± 1.0	55.1 ± 2.8	128 ± 6.0	202 ± 10	94.1 ± 4.7	91.2 ± 4.6
SPIRE 250 μm^d	9.8 ± 0.7	65.5 ± 4.7	72.2 ± 5.1	15.9 ± 1.1	4.8 ± 0.4	15.6 ± 1.1	32.4 ± 2.3	71.2 ± 5.1	96.7 ± 6.9	42.4 ± 3.0	56.3 ± 4.0
SPIRE 350 μm^d	4.4 ± 0.3	30.6 ± 2.2	30.8 ± 2.2	8.0 ± 0.6	2.1 ± 0.2	8.7 ± 0.6	13.7 ± 1.0	31.7 ± 2.3	37.6 ± 2.7	16.4 ± 1.1	28.4 ± 2.0
SPIRE 500 μm^d	1.9 ± 0.1	13.3 ± 1.0	12.6 ± 0.9	3.5 ± 0.3	0.8 ± 0.1	4.2 ± 0.3	5.3 ± 0.4	14.6 ± 1.0	14.4 ± 1.0	6.3 ± 0.4	13.9 ± 1.0

^aParameters of the photometric apertures used to derive *Herschel* flux densities. $2a$ and $2b$: lengths of the major and minor axes; α : position angle of the aperture's major axis measured east of north.

^bFrom Dale et al. (2007).

^cFrom the SCANPI tool and the HIRES atlas (see text).

^dFrom D12.

IRAS High Resolution Image Restoration (HIRES, Surace, Sanders & Mazzarella 2004) atlas. We provide the MIPS, PACS and SPIRE flux densities in Table 2. MIPS and PACS fluxes are in very good agreement. We refer to D12 for quantitative comparisons between MIPS and PACS global fluxes at 70 and 160 μm .

Cold dust temperatures are often derived using single-MBB fits. Nevertheless, a galaxy contains a range of dust temperatures that a single MBB will not be able to capture. The warm dust component, in particular, spans a narrow range of dust temperatures, from ~ 40 to 100 K, and contributes to a non-negligible fraction of the 70 μm emission. As a result, using a single-MBB-model fit usually leads to an overestimation of the cold dust temperatures. We note that this effect particularly affects objects showing an enhanced 24–70 μm emission linked with stochastically heated grain emission, like the Magellanic Clouds (Bot et al. 2004; Bernard et al. 2008). We thus carry out a two-temperature modelling of our galaxies in order to separate the warm and the cold components, using the MIPS, PACS and SPIRE flux densities listed in Table 2 along with MIPS 24 μm and IRAS 25, 60 and 100 μm flux densities. We fit the data d_ν with a model of the form

$$d_\nu = A_w [\lambda^{-2} B_\nu(T_w)] + A_c [\lambda^{-\beta_c} B_\nu(T_c)], \quad (3)$$

with B_ν the Planck function and the five free parameters of our model: β_c is called the emissivity index of the cold component, T_w and T_c are the temperatures of the warm and cold components, respectively, and A_w and A_c are the overall amplitudes of each dust component (see discussion on the naming convention in the next section). This equation assumes optically thin emission over our wavelength range. As can be observed in equation (3), we choose to fix the emissivity index of the warm dust component in order to limit the number of free parameters in our model. We decide to fix β_w to 2.0. This is a good approximation of the opacity of the graphite/silicate dust models of Li & Draine (2001). We note that our choice of β_w does not influence the cold dust temperatures. Fixing β_w to 1.5 leads to a small decrease in the cold dust temperatures of less than 0.6 per cent if $\beta_c = 2.0$, and less than 1.6 per cent if β_c is free. Tabatabaei et al. (2011) (see also Tabatabaei et al., in preparation) have synthesized the two-MBB approach for M33,

with β_c free and β_w fixed to 2.0, 1.5 and 1.0, and found that $\beta_w = 2.0$ best reproduces the observed fluxes, reinforcing our choice.

We compute the expected photometry for the fitted model by convolving this model with the instrumental spectral responses of the different cameras. We refer to the individual user's manuals of each instrument for the usual conventions used for each instrument. We use the IDL function MPCURVEFIT (Markwardt 2009) to perform a Levenberg–Marquardt least-squares fit of the data. We weight the data during the χ^2 minimization in order to take the uncertainties on flux measurements into account.

3.3 Uncertainties on the parameters

Shetty et al. (2009) among others show that fits performed solely in the Rayleigh–Jeans regime are very sensitive to instrumental errors. Fits using the full far-IR-to-submm coverage usually lead to a significantly better determination of dust properties than fits only performed near the SED peak. In order to quantify the uncertainties on the parameters driven by the errors of our individual fluxes, we perform Monte Carlo simulations for each galaxy. We generate 500 sets of modified constraints. Each flux randomly varies within its error bar, following a normal distribution around its nominal value. The absolute calibration is correlated across the three SPIRE bands (see the SPIRE Observers' Manual), namely flux densities in the three bands are expected to move in the same direction if the absolute calibration would be revised. To account for this correlation, we vary the three SPIRE measurements consistently, that is, they are not allowed to vary relative to each other. We finally apply our two-temperature fit to these 500 modified data sets.

3.4 Global dust temperature and emissivity index

Fig. 2 shows the global SEDs we obtained. β_c is a free parameter in those models. We overlay the SCUBA data on our SEDs when available (indicated with the open circles in Fig. 2). Some of the SCUBA maps do not fully cover the outer part of the galaxies or show a poor detection at the rim of the discs due to a possible removal of diffuse emission during the data reduction. Those data

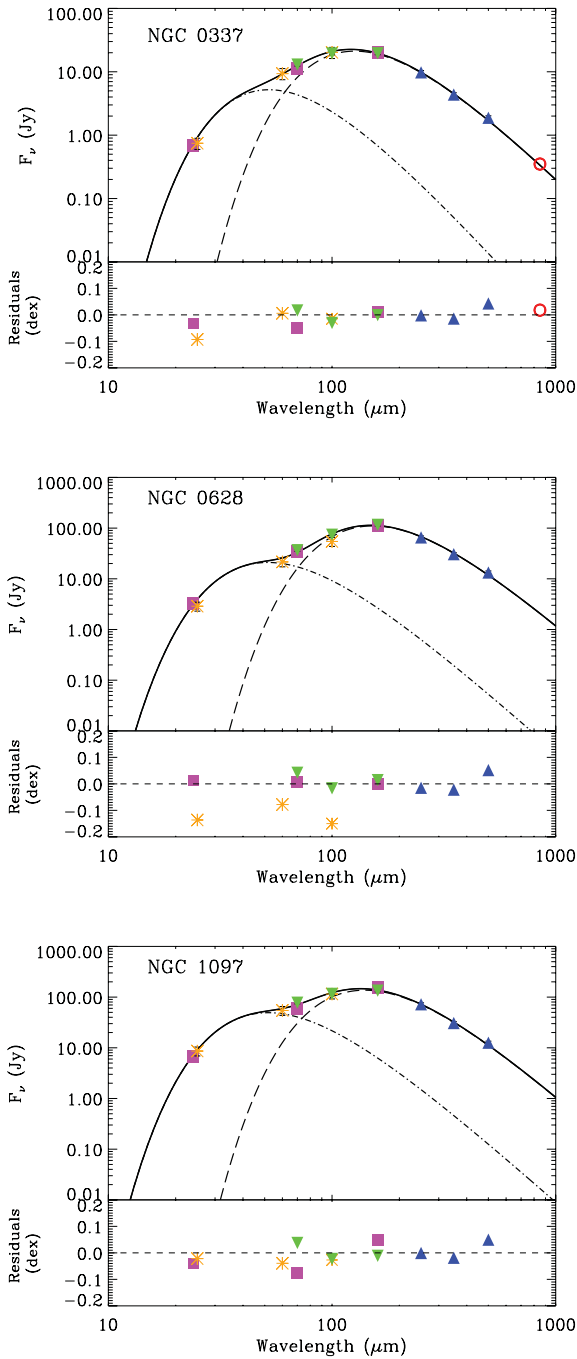


Figure 2. Global SED of our galaxies performed using a two-temperature fit. The emissivity index β_w of the warm component (dot-dashed line) is fixed at 2.0 and the emissivity index β_c of the cold component (long-dashed line) is a free parameter. *IRAS* (asterisks), *MIPS* (squares), *PACS* (downward triangles) and *SPIRE* (upward triangles) data are overlaid. *SCUBA* 850 μm flux densities are indicated with the empty circles but not used in the fit. If the error bars are not shown, errors are smaller than the symbols. The fitted β_c and temperatures are given in Table 3. The bottom panel of each plot indicates the residuals from the fit. See Section 3.1 for details on the modelling technique.

are not used in the modelling. The bottom panel for each galaxy indicates the residuals from the fit in logarithm scale. The differences in shape of the SEDs we obtain highlight the wide range of local ISM environments covered by the sample. Discrepancies par-

ticularly appear on the Wien side of the SEDs. We, however, note that the warm component does not significantly affect the fit to the long-wavelength cold component. The 100-to-24 μm flux density ratios vary from ~ 17 for NGC 1097 to ~ 37 for NGC 4826, thus from active to quiescent star-forming galaxies. Our SEDs mostly peak at similar wavelengths, residing between $\lambda = 117 \mu\text{m}$ for NGC 337 and $\lambda = 165 \mu\text{m}$ for NGC 1512, in their F_ν SEDs. We indicate the contribution of the warm component to the 70 μm fluxes in Table 3. This contribution can be higher than 50 per cent in some objects, legitimizing the necessity of two dust components in our simple approach. We also note that the relative flux at 60 and 70 μm influences the fits as it samples the SEDs where the warm and cold dust overlaps. We try to fit our data excluding the *IRAS* 60 μm data. This leads to a decrease in our cold dust temperature by less than 1.8 per cent if β_c is fixed to 2.0 and less than 8.7 per cent if β_c is free.

We summarize the median values of T_c and β_c in Table 3, with their errors, namely the standard deviation of the parameter distribution obtained using the Monte Carlo simulations. We also indicate the cold dust temperatures obtained with an emissivity index β_c fixed to a standard value of 2.0 for comparison. The median reduced chi-squared value is ~ 1.4 when β_c is fixed to 2.0 and ~ 1.1 when β_c is free, which means that both models lead to satisfying fits. When β_c is free, we observe variations of the cold dust emissivity within our sample, with values ranging from 0.8 to 2.5 (Table 3). Those values are consistent, within the uncertainties, with the emissivity index ranges quoted in the literature (Hildebrand 1983; Dupac et al. 2003, among others). We note that using a free emissivity index also increases the uncertainties on the temperature estimates.

Fig. 3 enables us to visualize the distribution of the 500 runs, results of the Monte Carlo simulations, for each galaxy in a T_c - β_c parameter space. In all panels, the green crosses are (T_c, β_c) combinations derived from 500 fits taking the correlation between *SPIRE* calibration uncertainties into account. For comparison, we also plot with the black crosses the (T_c, β_c) combinations obtained if *SPIRE* data are allowed to vary independently of each other. The median values of the temperatures and emissivity indices are annotated in red. We remind the reader that those are the median values reported in Table 3. The last panel gathers the individual trends. Those trends are obtained by taking the average every 30 runs. We note that, as expected, taking into account the correlations between *SPIRE* calibration uncertainties narrows the ranges of values reached by the parameters. Nevertheless, this assumption does not change the median values of T_c and β_c obtained (less than 2 per cent difference). We observe a clear T_c - β_c anticorrelation in all panels of Fig. 3. Shetty et al. (2009) caution against the interpretation of the inverse T_c - β_c correlation as a physical property of dust in the ISM since it could be created by measurement uncertainties. Our results clearly confirm that fitting SEDs to noisy fluxes, even with data sampling the thermal dust emission from 24 to 500 μm , leads to a T_c - β_c anticorrelation. We further discuss this effect in the following section.

4 MAPPING THE COLD DUST TEMPERATURE AND EMISSIVITY

4.1 Dust temperature distribution – β_c fixed

The spatial resolution of the *Herschel* instruments now enables us to reproduce the previous study on a local basis in order to resolve the dust temperature and emissivity within galaxies and directly link them with other ISM tracers. We use our two-temperature fitting

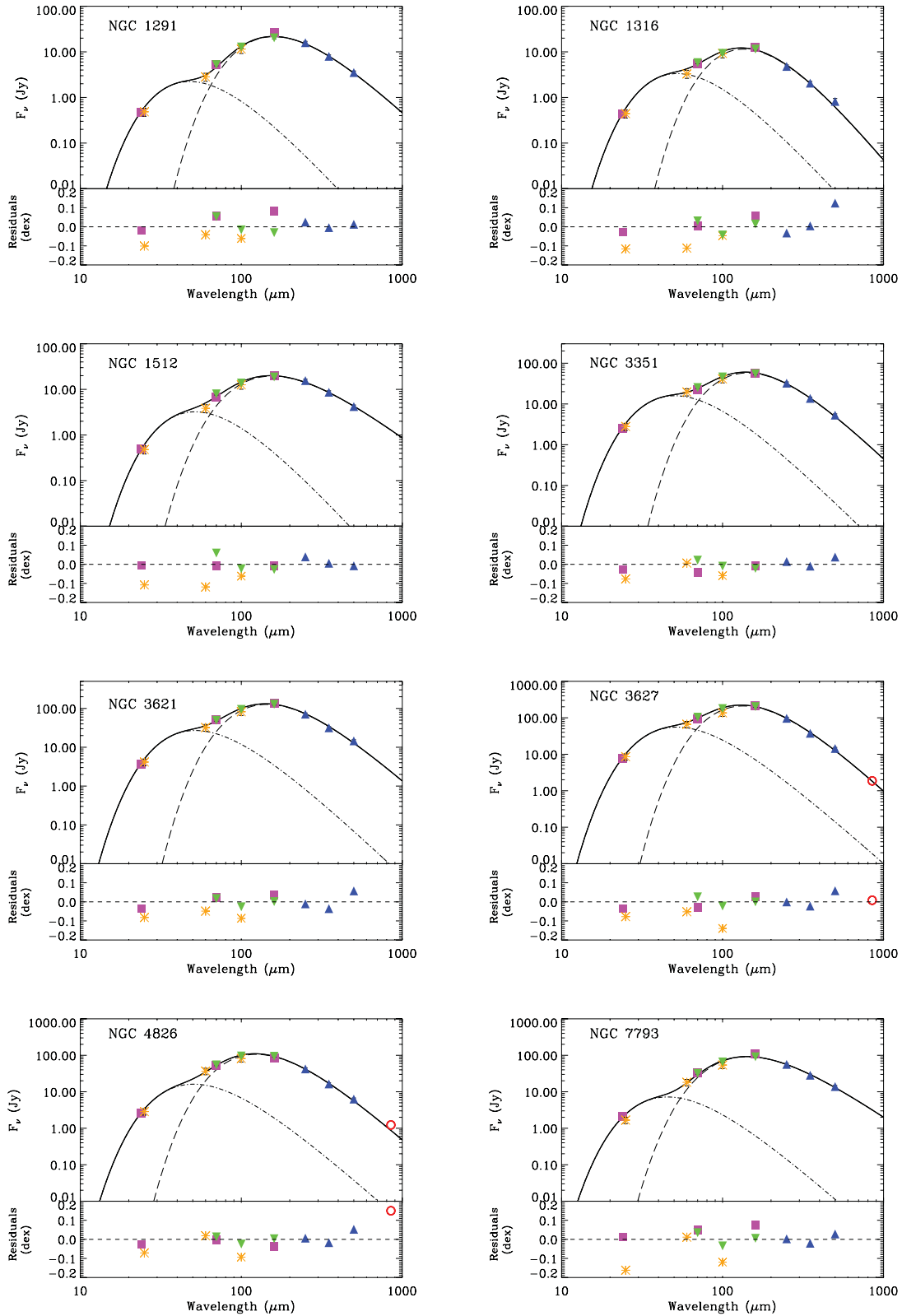


Figure 2 – continued

approach to derive maps of dust temperature and dust emissivity in our objects. In order to constrain the warm dust emission, we use *Spitzer*/MIPS images at 24, 70 and 160 μm . These maps were obtained as part of the SINGS programme (Kennicutt et al. 2003)

and reduced using the SINGS Fifth Data Delivery pipeline. MIPS, PACS and SPIRE maps are then convolved to the SPIRE 500 μm resolution (see Section 2.4 for the method) and projected to a common sample grid with a pixel size of 18 arcsec, thus half of the

Table 3. Best-fitting parameters.

	$\beta_c = 2$			β_c free			
	$L_{70\ \mu\text{m,warm}}/L_{70\ \mu\text{m,tot}}$	T_w (K)	T_c (K)	$L_{70\ \mu\text{m,warm}}/L_{70\ \mu\text{m,tot}}$	T_w (K)	β_c	T_c (K)
NGC 337	0.58	51.4 ± 1.7	21.3 ± 0.8	0.35	55.7 ± 14.3	1.6 ± 0.2	25.2 ± 2.4
NGC 628	0.53	55.9 ± 1.8	19.0 ± 0.4	0.52	56.0 ± 5.3	2.0 ± 0.2	19.1 ± 1.3
NGC 1097	0.57	55.8 ± 1.6	20.7 ± 0.6	0.57	55.9 ± 2.4	2.0 ± 0.2	20.7 ± 1.4
NGC 1291	0.57	56.2 ± 2.0	17.6 ± 0.4	0.36	60.8 ± 10.2	1.5 ± 0.2	20.4 ± 1.4
NGC 1316	0.32	58.9 ± 8.1	22.4 ± 0.8	0.52	55.2 ± 11.2	2.5 ± 0.4	19.4 ± 2.4
NGC 1512	0.81	49.9 ± 1.1	16.8 ± 0.5	0.38	56.4 ± 16.8	0.8 ± 0.2	25.1 ± 2.9
NGC 3351	0.51	57.6 ± 2.2	20.4 ± 0.5	0.53	57.4 ± 3.3	2.1 ± 0.2	20.0 ± 1.2
NGC 3621	0.54	54.9 ± 1.6	19.7 ± 0.5	0.47	55.9 ± 5.3	1.8 ± 0.2	20.7 ± 1.4
NGC 3627	0.32	59.2 ± 6.1	22.4 ± 0.6	0.47	55.8 ± 5.6	2.3 ± 0.2	20.2 ± 1.4
NGC 4826	0.21	59.1 ± 13.5	23.7 ± 0.7	0.24	57.0 ± 16.4	2.1 ± 0.2	23.1 ± 1.6
NGC 7793	0.59	51.9 ± 1.7	18.7 ± 0.5	0.17	63.4 ± 19.5	1.2 ± 0.2	24.4 ± 1.9

Note. The temperatures and emissivity indices given in this table are the median values of the Monte Carlo distributions (see Section 3.2).

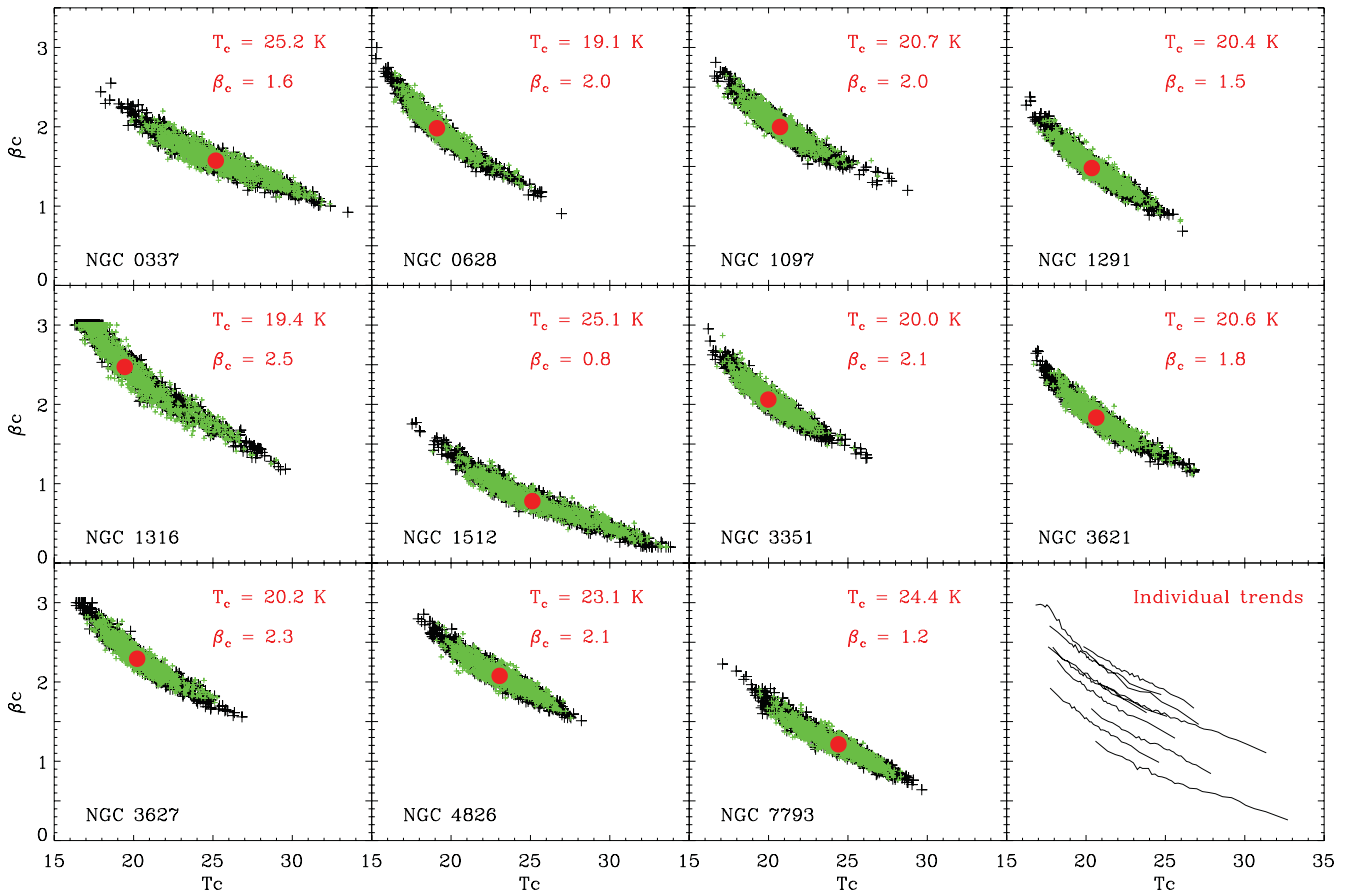


Figure 3. Distribution of the cold dust parameters in the temperature–emissivity index plane. 500 fits of randomly modified data sets were performed. The green crosses indicate the distribution when the correlation between SPIRE calibration errors was applied and the black crosses when no correlation was taken into account. The red dots indicate the median values on T_c and β_c . Those values are reminded in each panel. The last panel summarizes the trends of all the galaxies.

FWHM of SPIRE at $500\ \mu\text{m}$. This pixel size corresponds in linear scale to ISM elements ranging from ~ 340 pc for our closest galaxy NGC 7793 to ~ 1.8 kpc for the farthest galaxy of our sample NGC 1316. The emissivity of the warm component is fixed to a standard emissivity of 2.0. We first use a *fixed emissivity index for the cold dust component* to obtain a robust determination of the cold dust temperature distribution based on colour temperatures. We study the case with a free β_c in the following section.

We exclude pixels with flux densities below a 3σ detection limit in all bandpasses. Uncertainties on the fit parameters are derived on a local basis using Monte Carlo simulations as described in Section 3.2. We generate 100 sets of modified constraints per pixel and run our SED modelling technique on those sets. We average (median) the 100 dust temperature values obtained in each pixel and derive the final cold dust temperature map. We show the cold temperature map of NGC 3627 obtained with β_c fixed to a standard

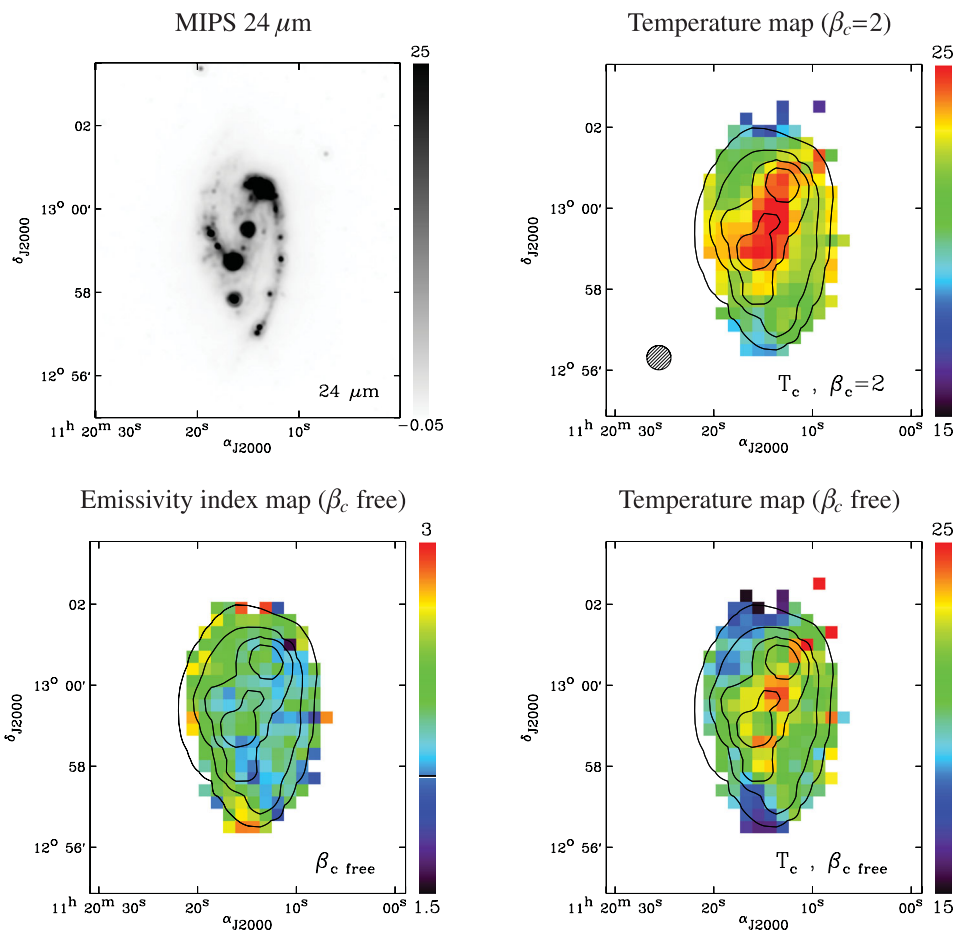


Figure 4. Upper left-hand panel: MIPS 24 μm image (in MJy sr^{-1}) of NGC 3627. Upper right-hand panel: cold dust temperature map of NGC 3627 (in K) derived using $\beta_c = 2.0$. We overlay the MIPS 24 μm contours (smoothed to the resolution of the temperature maps) for comparison. The FWHM of the PSF of SPIRE 500 μm is shown by the dashed circle. Lower left-hand panel: emissivity index map of NGC 3627 derived with T_c and β_c as free parameters. The value $\beta_c = 2.0$ is indicated on the colour scale. Lower right-hand panel: cold dust temperature map of NGC 3627 (in K) derived with T_c and β_c as free parameters. For each map, north is up and east is left. Temperature and emissivity maps for the rest of the sample are available in the appendix of this paper.

value of 2.0 in Fig. 4 (upper right-hand panel). We overlay the MIPS 24 μm contours on the maps to compare the temperature distribution with the star-forming regions of the galaxies whose 24 μm emission is a usual good tracer. We show the cold dust temperature maps of the whole sample in Fig. A1 (top middle panel for each galaxy). We observe a clear radial trend of dust temperatures in our objects. The temperature maxima coincide with the centre of the star-forming regions. The dust grain temperatures decrease in the outer parts of galaxies. This radial trend is consistent with results obtained with *Herschel* observations in nearby galaxies (Engelbracht et al. 2010; Boquien et al. 2011; Bendo et al. 2012; Hinz et al. 2012).

The source of heating of the cold dust is still poorly understood. The emission of old stars, traced by the IRAC 3.6 μm observations, smoothly decreases with radius, at our resolution, in our objects. A radial trend of dust temperatures may thus suggest that the old stellar populations could contribute to the heating of the cold dust, while the youngest star-forming population is closely associated with the warm dust (Calzetti 2007). However, the star formation activity of our galaxies tends also to decrease radially in some of our objects as suggested by the 24 μm emission, and the resolution of our dust temperature maps may not allow us to properly disentangle between the different possible heating sources. We observe none the less that the cold dust temperature distribution follows the bars

in the galaxies NGC 1097 and 3627 or strongly peaks in the nucleus of NGC 1316 where the 24 μm emission peaks as well (see Fig. A1, top left-hand panels), suggesting a more significant role of the star-forming regions than the interstellar radiation field in heating the cold dust in those objects.

A12b perform a pixel-by-pixel SED modelling of the whole KINGFISH sample using the DL07 dust models on *Spitzer* + *Herschel* data up to 500 μm . These models couple a ‘PDR component’ reproducing the emission of PDRs with a range of radiation fields and a ‘diffuse ISM component’ exposed to a single radiation field intensity U_{min} . We note that in this model most of the cold dust is expected to reside in the diffuse component.

The energy absorbed by a cold grain in this diffuse phase is

$$\Gamma_{\text{abs}} \propto \int_0^{\infty} Q_{\text{abs}}(\lambda) U_{\lambda}(\lambda) d\lambda \propto U_{\text{min}}, \quad (4)$$

with Q_{abs} the absorption efficiency of the grains and U the intensity of the radiation field of the diffuse ISM, thus U_{min} .

The energy emitted by a cold grain in this diffuse phase is

$$\Gamma_{\text{em}} \propto \int_0^{\infty} \nu^{\beta} B_{\nu}(T_{\text{eq}}) d\nu \propto T_c^{4+\beta}, \quad (5)$$

with B_{ν} the Planck function and T_{eq} the equilibrium temperature in the phase, namely the temperature of the cold dust T_c .

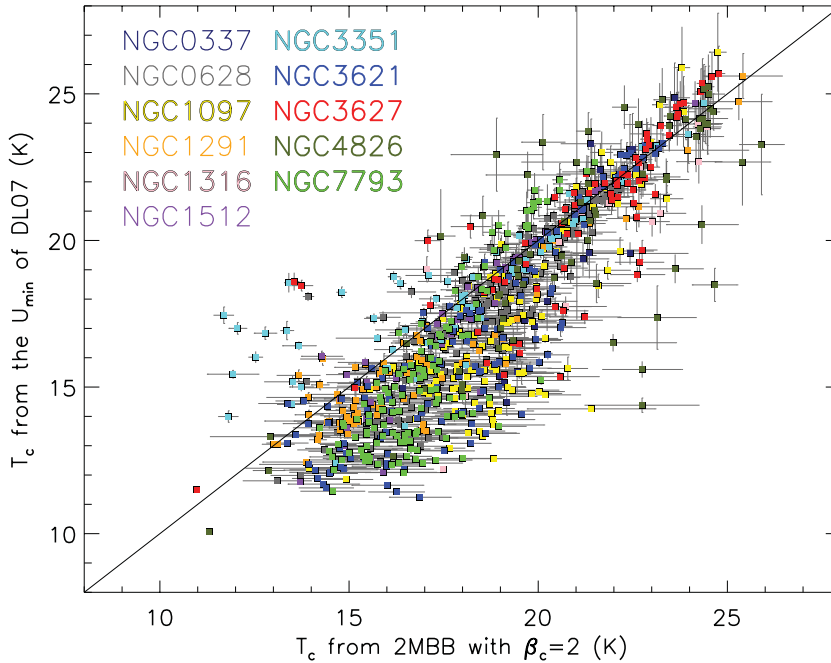


Figure 5. Comparison between the cold dust temperature obtained with our two-MBB models and the cold dust temperature derived from the radiation field of the diffuse ISM component (U_{\min}) from the DL07 models. The squares are pixel-by-pixel values (pixel size: 18 arcsec) averaged 4-by-4 for clarity. The line indicates a ratio of unity.

Assuming thermal equilibrium conditions, we can write that $\Gamma_{\text{abs}} = \Gamma_{\text{em}}$. We can thus associate the radiation intensity U_{\min} and the cold dust temperature T_c . If we assume that dust grains possess an emissivity index $\beta = 2.0$ and normalize the temperature to the equilibrium dust temperature of the Galaxy (17.5 K, Boulanger et al. 1996), we obtain

$$T_c(K) = 17.5 \times U_{\min}^{1/(4+\beta)} = 17.5 \times U_{\min}^{1/6}. \quad (6)$$

We can thus compare our derived cold temperature maps obtained with a fixed emissivity $\beta_c = 2.0$ with the U_{\min} map obtained by A12b using this formula. Dust temperatures have very similar distributions in both cases. We plot the pixel-by-pixel comparison in Fig. 5. We observe that in regions showing a ‘hotter’ cold dust temperature (co-spatial with star-forming regions or high starlight intensities), the temperatures obtained in both cases are very similar. The points diverge in regions that show a lower dust temperature, with colder temperatures deduced using the U_{\min} parameter obtained from DL07 and the conversion of equation (6). This could be explained by the fact that the DL07 model assumes a range of dust temperatures and thus allows to reach colder dust than a MBB fit with β_c fixed to 2.0. Our hypothesis of an emissivity index of $\beta = 2.0$ to translate U_{\min} into temperatures slightly influences our results but not enough to explain the trend we observe. We refer to A12b for a complete description of the U_{\min} maps for the whole KINGFISH sample.

We also derive temperature maps with an emissivity index of the cold dust component fixed to $\beta_c = 1.5$ and 1.0. This choice does not modify the relative distribution of cold dust temperatures in our objects but influences the temperature ranges obtained, scaling temperatures to higher values than in the ‘ $\beta_c = 2.0$ ’ case. We want to compare this effect in bright star-forming regions as well as in more quiescent regions. We separate our pixels into two different categories based on their SFR, using the MIPS 24 μm band as a qualitative indicator for the SFR and the relation from Calzetti

(2007):

$$\text{SFR}(M_{\odot} \text{ yr}^{-1}) = 1.24 \times 10^{-38} [L(24 \mu\text{m}) (\text{erg s}^{-1})]^{0.88}. \quad (7)$$

We fix the separation between active and less active regions at $\text{SFR} = 4 \times 10^{-3} M_{\odot} \text{ yr}^{-1} \text{ kpc}^{-2}$ and plot the variations of dust temperatures as a function of emissivity index in Fig. 6. The left-hand panel indicates the dust temperatures obtained from integrated fluxes using $\beta_c = 1.0, 1.5$ and 2.0. Galaxies are colour-coded. The errors are derived from our Monte Carlo simulations performed on global fluxes (Section 3.2). The middle panel shows the median values of the pixel-by-pixel dust temperatures if we restrict the study to the bright star-forming regions of the galaxies. The right-hand panel shows the median values of the pixel-by-pixel dust temperatures if we restrict the study to the more quiescent regions of the galaxies. For the middle and right-hand panels, errors are the standard deviations of the distributions of dust temperatures.

As mentioned earlier, we observe that using a lower emissivity index β_c shifts the temperature range to higher values. The median temperatures of bright star-forming regions are systematically higher than the median temperatures of more quiescent regions, as intuitively expected. With $\beta_c = 1.5$, the temperatures increase by up to 25 per cent for the bright regions and by up to 21 per cent for quiescent regions. With $\beta_c = 1.0$, the temperatures increase by up to 51 per cent for the bright regions and by up to 48 per cent for less active regions. The choice of β_c has a major impact on the dust temperatures obtained and on the dust masses usually derived from those blackbody fits (see Section 4.3). Our comparison between quiescent and active regions seems to indicate that the choice of β_c has a non-linear influence on the dust temperatures derived, with a slightly larger impact in bright regions.

4.2 Investigations on emissivity index variations

The coverage and resolution of *Herschel* enable us for the first time to properly constrain the submm slope of resolved SEDs, allowing

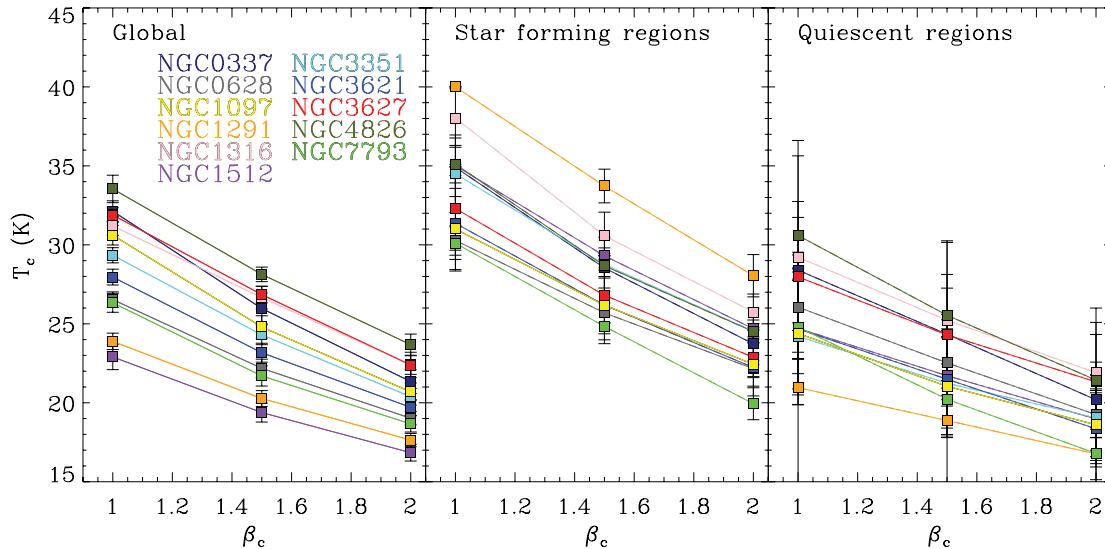


Figure 6. Dependence of the dust temperatures on the chosen cold emissivity index. Left-hand panel: global T_c obtained using $\beta_c = 1, 1.5$ and a standard emissivity index of 2.0. The galaxies are colour-coded. Middle panel: median of the pixel-by-pixel T_c obtained for star-forming regions. Right-hand panel: median of the pixel-by-pixel T_c obtained for less active regions.

for more complex analysis of potential variations in dust emissivity at local scale. To investigate these variations, we apply the same local MBB fitting technique *with both T_c and β_c as free parameters*. We show the emissivity index map and the cold temperature map of the galaxy NGC 3627 obtained with those assumptions in Fig. 4 (lower panels). We gather the cold dust temperature maps of the whole sample in Fig. A1 (middle panel in each row for each galaxy). We overlay the MIPS 24 μm contours as a comparison. The same colour scale is used for the two cold dust temperature maps. We note that the choice of β_c (2.0 or free) strongly influences the cold dust temperature ranges obtained for NGC 337 and 7793. We used different colour scales for these galaxies.

Temperatures – Choosing β_c as a free parameter modifies the temperature distribution in our galaxies. The dust temperature distribution is less homogenous in the outer parts of galaxies (in NGC 628 or 1097, for instance). This is probably linked to the fact that our model becomes very sensitive to noise at low surface brightnesses and was previously observed in Ade et al. (2011b) for the Large Magellanic Cloud (LMC) and in Foyle et al. (2012) for M83. When β is used as a free parameter in our model, we observe that the distribution of cold dust temperatures follows a systematic behaviour with the morphology of the galaxy. Barred spiral galaxies such as NGC 1097, 1291, 1512, 3351 and 3627 show distributions of their dust temperature map similar to those obtained with a fixed β_c , that is, a distribution that follows the star-forming regions or that is decreasing in the outer part of the galaxies. NGC 3627 presents an enhancement of the dust temperature at the end of its bar. Bars alter the abundance distribution of the gaseous component in galaxies (Friedli, Benz & Kennicutt 1994) and affect the star formation activity (Ellison et al. 2011). Strong concentrations of molecular gas are detected at the end of the bar of NGC 3627 (Warren et al. 2010) which is probably responsible for the high star formation activity and thus for the high dust temperature observed. In contrast, the grand-design spiral NGC 628 or bulgeless objects like NGC 3621 or 7793 show cold dust temperatures that are homogenous throughout the structure of the galaxies. The fact that the cold dust temperature distribution does not seem to correlate with any dust heating source (neither star-forming regions nor old stellar popula-

tions or radius) within the galaxies is worrying and questions the use of a free β_c in the model, at least for this type of galaxy.

Emissivities – Here again the emissivity index maps seem to show a distribution that depends on the morphology of the galaxy. Barred spiral galaxies show a homogeneous distribution of emissivity index, with median values similar to the β_c values determined globally. In contrast, we observe a radial decrease in emissivity index in the non-barred galaxies NGC 628, 3621 or 7793 when β_c is free. This radial decrease in β_c was also observed in M33 by Tabatabaei et al. (2011) or in the Andromeda Galaxy (also known as M31) by Smith et al. (2012). We nevertheless note a clear inverse relation between temperature and emissivity index in some of these objects. We discuss this further in the following section. We do not observe a clear trend in NGC 337 and 4826. Finally, we obtain low local emissivity values for the galaxies NGC 337 and 7793 compared to the standard value of 2.0 as shown by the emissivity index range of each map. These low emissivity indices are consistent with the integrated values obtained at global scale. Indeed, we find global emissivity indices β_c of 1.6 and 1.2 for NGC 337 and 7793, respectively.

T_c - β_c anticorrelation – Fig. 7 gathers pixels that show a detection above our signal-to-noise ratio threshold in each *Herschel* band for our 11 galaxies in a T_c - β_c diagram. Global values of Table 3 are also overlaid with stars. We estimate the errors using the standard deviation of the Monte Carlo simulations of uncertainties performed for each pixel. They include calibration and sky background uncertainties. An anticorrelation is clearly observed between temperature and emissivity, with higher emissivity values in colder ISM elements. This relation is coherent with laboratory measurements (Mennella et al. 1998; Meny et al. 2007, and references therein) that have reported a strong dependence between the temperature and the spectral index of the absorption coefficients, with higher β values found for dust grains in cold cores. The anticorrelation between T_c and β_c does not disappear if we restrict ourselves to the pixels showing the smallest uncertainties. This might indicate that Eddington bias (i.e. uncertainties on measurements) could not be sufficient to explain the anticorrelation we observe, even if this assumption is difficult to assess. The discrepancies between the temperature maps derived with a fixed and a free β_c , with temperature distributions

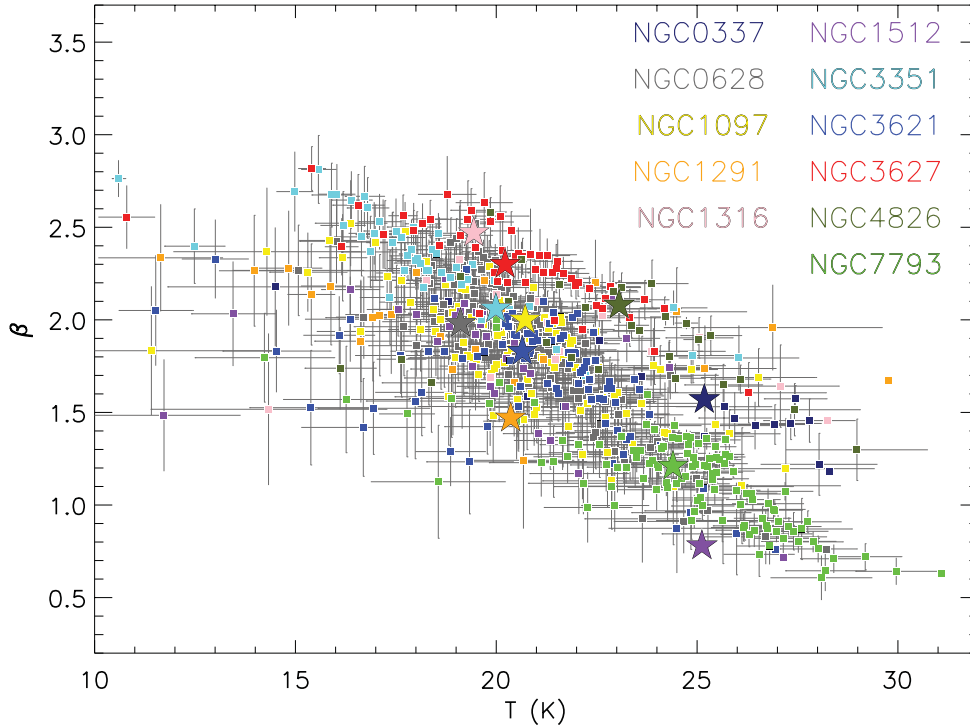


Figure 7. Temperature dependence of the spectral index in our sample. Global estimates are shown with the stars. The squares are pixel-by-pixel values (pixel size: 18 arcsec) averaged 4-by-4 for clarity.

not correlated with potential dust heating sources in non-barred galaxies, and the well-known degeneracy between temperature and emissivity index of course questions the physical sense of letting both temperature and emissivity vary at the same time. We also caution the fact that even with the good resolution of *Herschel* instruments, the ISM elements studied in an 18×18 arcsec² pixel are large for the galaxies of the sample, even for our closest object (~ 0.3 kpc for NGC 7793). We thus probe a large mixture of dust temperatures for each ISM element. It can therefore be challenging to disentangle a real relation or an anticorrelation created by the addition of several dust temperatures, with an ‘artificial’ flattening of the slope when cold dust is present along the line of sight. We refer to Juvela & Ysard (2012) for a detailed analysis of the possible effect of temperature mixing on the T – β relation. A compromise to avoid these degeneracies for our non-barred galaxies could be to use β as a free parameter to derive an average emissivity index across the galaxy and then fix β to this value to derive temperature and mass surface density maps (as done in Abergel et al. 2011, for instance). Studies on resolved structures in the Milky Way (e.g. Paradis, Bernard & Mény 2009) or in closer galaxies like the Magellanic Clouds are necessary to restrict the dust temperature range probed per resolved element and contribute to resolve these issues.

5 DUST MASSES

5.1 Dust mass maps

Since most of the dust mass of a galaxy resides in its cold phase, we can directly derive dust mass maps from the cold temperature maps previously generated. To do so, we use the relation

$$M_{\text{dust}} = \frac{S_{\nu_0} D^2}{\kappa_{\nu_0} B_{\nu_0}(T_c)} \quad (8)$$

with S_{ν} the flux density, ν_0 the reference frequency, κ_{ν_0} the absorption opacity of dust grains at that reference frequency, D the distance from the galaxy and $B(T_c)$ the Planck function for a given temperature T_c . D12 derive global dust masses of the KINGFISH sample from MBBs using the reference frequency $\nu_0 = c/250 \mu\text{m}$ and the SPIRE 250 μm flux densities. Similar techniques have been used to derive dust mass surface density maps in very nearby galaxies by Foyle et al. (2012) for M83, Parkin et al. (2012) for Centaurus A or Mentuch Cooper et al. (2012) for the Whirlpool system. Since the 500 μm band is less sensitive to temperature variations than the 250 μm band, we prefer to use $\nu_0 = c/500 \mu\text{m}$ as the reference frequency. We note that using 500 μm as a reference wavelength for dust calculation could make our masses dependent on submm excess if present in our objects. However, we do not expect submm excess to be significant at 500 μm for our selection of galaxies (mostly metal-rich objects). We choose a dust opacity $\kappa_{\text{abs}}(250 \mu\text{m}) = 3.98 \text{ cm}^2 \text{ g}^{-1}$ (taken from www.astro.princeton.edu/~draine/dust/dustmix.html) and for each case (β fixed or free) derive $\kappa_{\text{abs}}(500 \mu\text{m})$ such as

$$\kappa_{\text{abs}}(500 \mu\text{m}) = \kappa_{\text{abs}}(250 \mu\text{m}) \times \left(\frac{500}{250} \right)^{-\beta}. \quad (9)$$

We show the dust mass surface density map obtained for the galaxy NGC 3627 with $\beta_c = 2.0$ and β_c free (in $M_{\odot} \text{ kpc}^{-2}$, log scale) in Fig. 8. We overlay MIPS 24 μm contours for comparison. We gather the dust mass surface density maps (with $\beta_c = 2.0$ and free) for the whole sample in Fig. A1 (right-hand panels for each galaxy). We observe that peaks of this distribution are usually located in the centre of the galaxies (e.g. NGC 337 and 3351). Nevertheless, peaks are also found at the bar-ends in NGC 3627, coinciding with peaks in the molecular hydrogen detected through CO observations (Leroy et al. 2009), linking the dust concentrations with the cold gas reservoirs. This result is similar to that of Foyle et al. (2012) who find that the highest dust concentration in M83

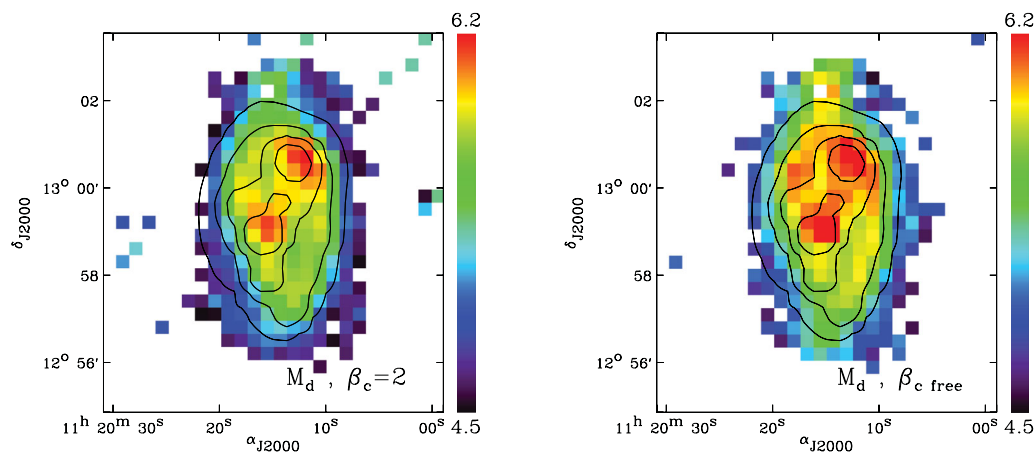


Figure 8. Dust mass surface density map of NGC 3627 (in $M_{\odot} \text{ kpc}^{-2}$, log scale) derived with $\beta_c = 2.0$ (left-hand panel) and β_c free (right-hand panel). We overlay the MIPS 24 μm contours for comparison. The dust mass surface density maps for the rest of the sample are available in the appendix of this paper.

is located in the nucleus and at the ends of the bar of the galaxy. We observe peaks of the dust mass surface density in the north-eastern and south-western arms of NGC 1512, here again at the end of the bar where the dust emission peaks from *Spitzer*/IRAC to *Herschel*/SPIRE wavelengths. Unfortunately, no CO observations are available for this galaxy that would allow comparisons with the molecular gas distribution. We observe high concentrations of dust at the north-west and south-east sides of the nucleus in NGC 1316, which correspond to peaks of dust emission at PACS and SPIRE wavelengths (see the resolved blobs in Fig. 1). These dusty structures coincide with reservoirs of molecular hydrogen detected in CO (Lanz et al. 2010). Horellou et al. (2001) have suggested that this molecular gas could have an external origin (accretion of material during merging processes). We, however, remind the reader that NGC 1316 possesses a low-luminosity X-ray AGN. Our submm wavelengths thus potentially contain non-thermal emission from the AGN that could affect the SEDs and the dust mass map we obtain, as discussed in Bendo et al. (2012) for M81 or in Parkin et al. (2012) for Centaurus A. A refinement of our resolved fit combining non-thermal emission from the AGN and dust associated with the X-ray bubbles would be necessary to understand how this influences the distribution of the dust mass surface density in this object.

We note that a non-negligible amount of dust is detected in the ring of NGC 1291, with higher dust mass surface densities than in the nucleus in the western arm in particular. van Driel, Rots & van Woerden (1988) observations of H I in this galaxy have revealed a concentration towards the ring and a central hole in the distribution. Dust thus seems to trace the atomic gas in this galaxy. A proper comparison of the ring/nucleus temperature and masses in NGC 1291 is detailed in Hinz et al. (2012) We finally note that the choice of β_c (fixed or free) does not affect the locations of the dust mass surface density peaks in our galaxies but directly influences the total dust masses derived for each galaxy, as discussed in the following section.

5.2 Dependencies of the derived total dust masses

In this final section, we aim to quantitatively compare the total dust mass derived for our objects with the different modelling methods used in this paper. Table 4 summarizes the total dust masses obtained by adding the individual dust masses determined pixel by

pixel with our two-MBB modelling technique in the four different cases $\beta_c = 2.0, 1.5, 1.0$ or free. The global fit section indicates the total dust masses calculated from temperatures derived with a two-MBB fit of the integrated fluxes. The errors on the dust mass are directly deduced from the temperature errors, the main source of uncertainties for our dust estimates. The non-linearity of the Planck function at IR wavelengths is translated into the asymmetric errors of our dust mass estimates. For the local MBB fits, the final errors are obtained by summing the individual uncertainties. A12b perform a pixel-by-pixel SED modelling of the KINGFISH galaxies using the DL07 model and produce dust mass maps for the whole sample. We sum up the local dust masses they obtain in the regions we selected (3σ detections in all *Herschel* bands) in our galaxies and add these values to Table 4 for comparison.

5.2.1 Influence of the emissivity index

Emissivity spectral indices ranging between 1.0 and 2.0 are commonly used in the literature. Table 4 highlights the strong dependence of the total dust mass estimate on the choice of β_c . Fig. 9 directly illustrates the decrease in dust mass with emissivity index. We note, for instance, that MBB fits using a cold dust emissivity index of 1.5 lead to a decrease in the total dust mass of ~ 50 per cent compared to those performed with a standard emissivity index of 2.0 and that MBB fits using an emissivity index as low as 1.0 will lead to a decrease of ~ 70 per cent. For NGC 337 and 7793, the distributions of dust temperatures and emissivity indices derived from the Monte Carlo simulations on integrated fluxes (see Fig. 3) seem to rule out the use of a single-temperature dust model with $\beta_c = 2.0$ to model the cold dust emission at global scale. At local scale, the cold dust emissivity maps of NGC 337 and 7793 show that β_c is always lower than 2.0, leading to the same conclusion. We note that a MBB fit with $\beta_c = 2.0$ is not a valid assumption at global scale for NGC 1512 either. The emissivity map does not, however, show such a trend at local scale. We conclude that the choice in the emissivity index value has a direct and significant impact on the dust mass deduced and thus on the interpretation made from these values (gas-to-dust mass ratios, for instance). It also complicates direct comparisons between studies that call for different models and assumptions.

Table 4. Global dust masses in units of $10^5 M_{\odot}$.

	Global fit			Sum of the dust masses obtained per pixel				
	$\beta_c = 2.0$	β_c free	D12 ^a	$\beta_c = 2.0$	$\beta_c = 1.5$	$\beta_c = 1.0$	β_c free	A12b ^b
NGC 337	361 ⁺²⁵ ₋₂₂	205 ⁺³⁸ ₋₂₈	225 ⁺⁷³ ₋₇₃	347 ⁺⁴⁶ ₋₃₇	180 ⁺¹⁸ ₋₁₆	94 ⁺¹² ₋₉	214 ⁺⁴⁰ ₋₃₂	240 ⁺⁶² ₋₆₂ (306)
NGC 628	441 ⁺²⁰ ₋₁₈	437 ⁺⁶⁶ ₋₅₂	291 ⁺³⁷ ₋₃₇	381 ⁺⁴⁶ ₋₃₆	207 ⁺²¹ ₋₁₇	113 ⁺¹¹ ₋₉	371 ⁺⁵⁵ ₋₄₆	329 ⁺⁵³ ₋₅₃ (355)
NGC 1097	1390 ⁺⁷³ ₋₆₆	1380 ⁺¹⁹⁰ ₋₁₅₂	904 ⁺²²⁹ ₋₂₂₉	1309 ⁺¹²¹ ₋₁₀₉	749 ⁺⁶⁹ ₋₆₇	415 ⁺³⁸ ₋₃₇	1420 ⁺²³¹ ₋₂₀₃	1241 ⁺²²⁶ ₋₂₂₆ (1338)
NGC 1291	283 ⁺¹⁴ ₋₁₃	151 ⁺²² ₋₁₇	293 ⁺⁷⁹ ₋₇₉	214 ⁺⁴⁵ ₋₃₉	127 ⁺²³ ₋₂₁	73 ⁺¹² ₋₁₀	241 ⁺⁴⁴ ₋₅₅	194 ⁺¹⁰⁶ ₋₁₀₆ (422)
NGC 1316	170 ⁺¹¹ ₋₁₀	312 ⁺⁹⁵ ₋₆₁	126 ⁺¹³ ₋₁₃	215 ⁺²² ₋₄₂	125 ⁺¹⁴ ₋₂₆	72 ⁺¹¹ ₋₁₇	186 ⁺³⁰ ₋₃₃	129 ⁺²¹ ₋₂₁ (183)
NGC 1512	462 ⁺³² ₋₂₉	95 ⁺²² ₋₁₅	164 ⁺¹⁹ ₋₁₉	250 ⁺³⁷ ₋₃₈	143 ⁺²⁰ ₋₁₈	81 ⁺⁹ ₋₁₀	195 ⁺³⁴ ₋₃₅	188 ⁺³⁵ ₋₃₅ (231)
NGC 3351	258 ⁺¹³ ₋₁₂	287 ⁺³⁷ ₋₃₀	196 ⁺²⁰ ₋₂₀	279 ⁺²⁸ ₋₂₂	160 ⁺¹⁴ ₋₁₁	91 ⁺⁹ ₋₆	468 ⁺⁷⁵ ₋₆₄	238 ⁺³⁴ ₋₃₄ (283)
NGC 3621	369 ⁺¹⁹ ₋₁₇	294 ⁺⁴⁰ ₋₃₂	242 ⁺⁸⁴ ₋₈₄	358 ⁺⁴⁴ ₋₃₆	191 ⁺²² ₋₁₈	103 ⁺¹⁶ ₋₁₂	283 ⁺³⁶ ₋₃₁	333 ⁺⁵⁸ ₋₅₈ (409)
NGC 3627	601 ⁺²⁹ ₋₂₇	892 ⁺¹²⁹ ₋₁₀₉	439 ⁺⁹⁷ ₋₉₇	571 ⁺²⁴ ₋₃₀	317 ⁺¹⁹ ₋₁₉	170 ⁺¹⁹ ₋₁₆	782 ⁺⁸⁰ ₋₆₆	475 ⁺⁹⁹ ₋₉₉ (543)
NGC 4826	76 ⁺⁴ ₋₄	85 ⁺¹² ₋₉	52 ⁺⁶ ₋₆	75 ⁺⁵ ₋₅	40 ⁺⁵ ₋₄	21 ⁺⁴ ₋₃	86 ⁺⁸ ₋₇	59 ⁺⁹ ₋₉ (61)
NGC 7793	140 ⁺⁸ ₋₇	49 ⁺⁷ ₋₆	131 ⁺²⁸ ₋₂₈	153 ⁺¹⁵ ₋₁₂	75 ⁺⁷ ₋₆	37 ⁺³ ₋₃	48 ⁺⁵ ₋₅	131 ⁺⁴² ₋₄₂ (145)

^aTotal dust masses derived by D12 using the DL07 model to fit the global SED.

^bThe dust mass maps are derived by A12b using the DL07 model applied pixel by pixel. The dust masses are derived adding the dust masses of pixels that are above our signal-to-noise ratio threshold. The total dust masses they derive (whole galaxy) are given in parentheses.

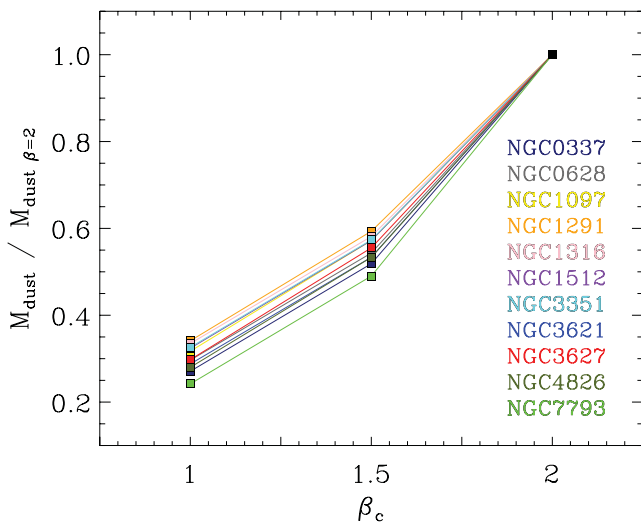


Figure 9. Dependence of the total dust mass on the cold dust emissivity index. The x-axis indicates the emissivity index in the modelling. Dust masses are normalized to those deduced with a standard emissivity index of 2.0.

5.2.2 Influence of the SPIRE data

Several studies have stressed the importance of observations longwards of 160 μm to properly determine dust temperatures and masses (Gordon et al. 2010). Galametz et al. (2011) show that metal-rich galaxies usually have dust SEDs that peak at long wavelengths and require constraints above 160 μm to position the peak and sample the submm slope of their SEDs and thus correctly probe the dust temperature distribution. On the other hand, metal-poor galaxies modelled with submm data could show higher dust masses than when modelled without submm data, due to the flattening of the submm slope or submm excess often detected in those objects. We can directly compare our dust masses derived with submm data to those derived with data up to the 160 μm constraint of *Spitzer*. We observe that dust masses obtained using *Herschel* data can dif-

fer from those derived with *Spitzer*-based fits available in Draine et al. (2007), especially for the galaxies NGC 337, 628, 1097 and 1316. Do we see any trend with metallicity? Most of the galaxies of the sample show a decrease in the total dust mass. NGC 1316, the most metal-rich galaxy of the sample, shows the second highest decrease in our dust masses. The total dust masses of NGC 3621 or 7793 – galaxies that have lower metallicities – are, in contrast, rather unaffected by the addition of *Herschel* data. Of course, any statistical interpretation of metallicity effects is rather hazardous for this small sample. Nevertheless, these trends with metallicity are consistent with the dependence expected from Galametz et al. (2011) and are already mentioned in the study of D12 performed for the whole KINGFISH sample. To test the influence of SPIRE data on the dust mass we obtain at global scale, we apply our two-MBB fitting procedure on data up to 250 μm or data up to 350 μm . The emissivity index is fixed to 2.0, 1.5 or 1.0. Fig. 10 shows how the total dust mass estimates evolve with the number of SPIRE submm data included in the fits. We observe that two-MBB fits with $\beta_c = 2.0$ performed with data up to 250 μm could differ from those derived using the complete SPIRE coverage by ± 10 per cent (-17 per cent for NGC 1512 due to the very flat submm slope of this object not sampled when we restrict the fit to data below 250 μm). A12a performed comparisons between dust masses derived with data up to 160 μm or data including the full SPIRE coverage for NGC 628 and 6946 and found similar values (difference of ~ 16 per cent and 10 per cent, respectively). This difference is even more pronounced with $\beta_c = 1.5$ or 1, reaching up to 30 per cent in the second case. We finally note that using a two-MBB fit and data up to 350 μm leads to a systematic underestimation of the dust mass (by up to 10 per cent) if β_c is fixed to 2 for the galaxies of our sample.

5.2.3 Comparisons with Skibba et al. (2011)

Skibba et al. (2011) have estimated dust masses for KINGFISH galaxies using single-MBB fits with an emissivity index β of 1.5 and, as in this study, SPIRE 500 μm flux densities as a reference wavelength in their dust mass calculation. From our global two-MBB fits with β_c fixed to 1.5, we obtain dust masses that are larger

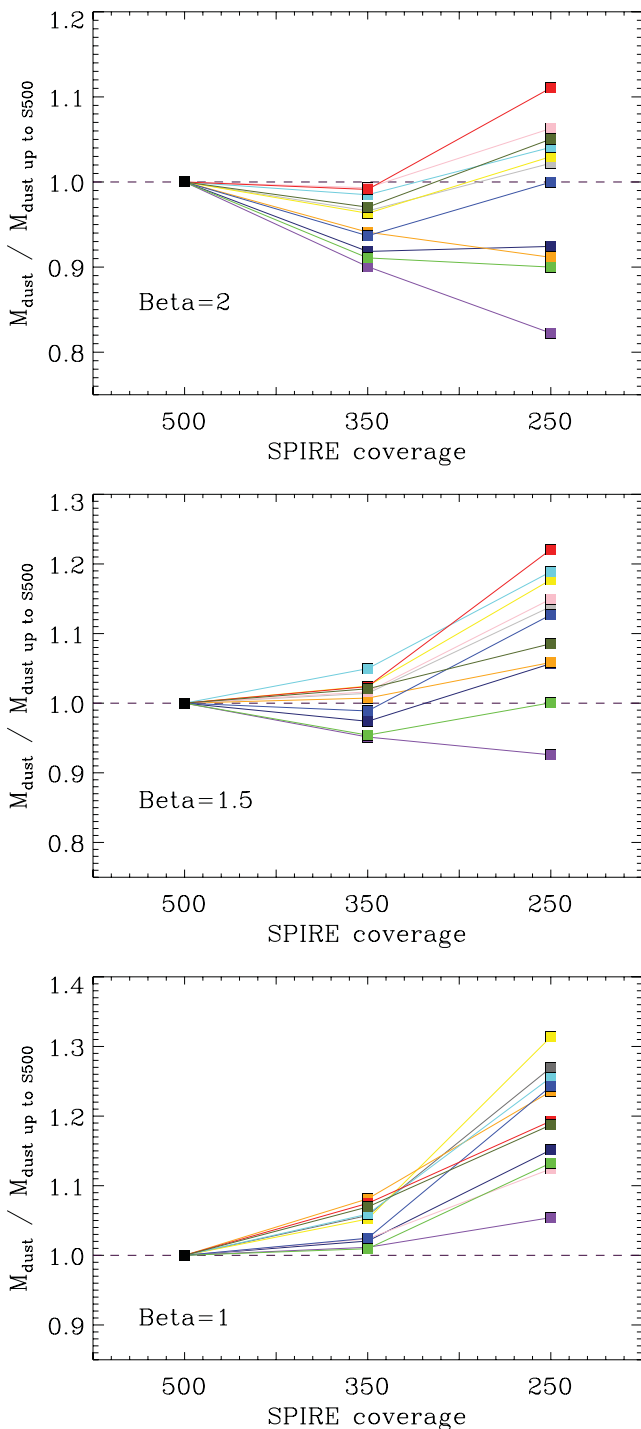


Figure 10. Dependence of the total dust mass on submm data included in the fits (two-MBB technique). The x -axis indicates the longest wavelength used. For instance, ‘350’ means that data from 24 to 350 μm are used. Dust masses are normalized to dust masses obtained using a complete coverage from 24 to 500 μm (called ‘ $M_{\text{dust up to } 500}$ ’). From the top to bottom, β_c was fixed to 2.0, 1.5 and 1.0. For the convention on galaxy colours, see Fig. 9.

by a factor of 1.1–2.6 than those obtained with the same cold dust emissivity index by Skibba et al. (2011). This is probably linked with their use of a unique MBB to fit the 70–500 μm range that leads to systematically higher temperature estimates for the cold dust (warm dust contributing to the 70 μm flux as mentioned in Section 3.4) and thus to lower dust masses.

5.2.4 Comparisons between MBB fits and the DL07 model

We observe that, and as already noted in D12, global dust masses derived with the DL07 model only differ from those derived with models using MBBs and a standard emissivity index of 2.0 by less than 35 per cent. A local estimation of the dust masses leads to similar results, namely an agreement within 30 per cent. It can be explained by the fact that in the wavelength range covered by SPIRE bands, the SED of the diffuse ISM component predicted by the DL07 model (corresponding to the bulk of the dust mass in these models) is quite similar to a single-temperature MBB with $\beta_c = 2$. We nevertheless note a significant difference between the dust mass obtained with a global fit for NGC 1512 when $\beta_c = 2.0$ and that obtained by D12. As mentioned previously, this galaxy shows a flat submm slope (global $\beta_c < 1.0$, Table 3). By fixing β_c to 2.0, we implicitly let our two-MBB model invoke colder dust to account for the SPIRE 500 μm emission. We observe that the DL07 model used to fit the global SED of this galaxy in D12 tends to underpredict the SPIRE 350 and 500 μm fluxes for this galaxy, which probably leads to an underestimation of the cold dust mass in this particular object. It is thus not surprising that we derive high dust masses for this galaxy. This could imply that cold dust could be present in this galaxy (and thus more dust mass), especially in the outer regions of the galaxy (not modelled in this study because of our signal-to-noise criterion), or that the global emissivity index is not well reproduced by standard graphite grains used to model carbon dust in the DL07 model.

5.2.5 Resolution effects

We want to compare our global dust masses with our resolved dust masses. In our local study, we restrict ourselves to regions above our signal-to-noise ratio threshold in all *Herschel* bands in our galaxies. Unfortunately, we are consequently missing dust mass in the faint outer parts of the galaxies. Making a direct comparison with the total dust mass derived from integrated fluxes and the sum of the individual dust masses obtained in the different pixels is thus not directly possible from this study. Nevertheless, we observe that the dust masses obtained globally using the DL07 model by D12 are systematically lower than those derived by summing the local dust masses (Table 4, last column, in parentheses) by 11 per cent for NGC 7793 to 69 per cent for NGC 3621, one of the lowest metallicity of the sample. Since dust masses derived using a MBB technique and an emissivity index of 2.0 are very close to those obtained using the DL07 model, we can easily predict the same effect for studies using MBBs, models that are intensively used by the scientific community. Those results agree with Galliano et al. (2011) who observe similar resolution effects while deriving dust masses in a strip of the LMC. The dust masses they derive from integrated fluxes are significantly lower than dust masses obtained from a local-scale study. The dilution of cold massive regions in hotter regions is invoked as a possible explanation of this effect. If this hypothesis is valid, we should expect an increase in our dust mass estimates until the resolution of our submm maps reaches scales where cold dust dominates (size of giant molecular clouds?). Observations at higher resolution, with ALMA, for instance, will help to address this issue. These differences of total dust mass estimates with resolution highlight the necessity of a resolved study to properly quantify the total dust mass budget of galaxies, when it is possible. The global dust mass of high-redshift galaxies might be underestimated because of lack of resolution. Moreover, our sample does not cover the full diversity of the SEDs of distant galaxies,

especially the very luminous IR galaxies detected at high redshift. In some cases, resolution effects may be even more significant. The choice of the fitting method therefore becomes decisive.

6 CONCLUSIONS

We combine *Spitzer*/MIPS and *Herschel* data to derive global properties of the cold dust in a sample of 11 nearby galaxies using a two-temperature fit to model their SEDs. At global scale:

(i) Our objects show a wide range of SEDs, with a clear evolution of the 100-to-24 μm flux density ratios from active to quiescent star-forming objects and variations in the global cold dust parameter β_c we derive, from $\beta_c = 0.8$ to 2.5.

(ii) We perform a Monte Carlo simulation in order to quantify the effect of uncertainties on the parameters derived from our fitting technique. We show that even with an exhaustive sampling of the global thermal dust emission, an artificial T - β anticorrelation can be created by uncertainties in the flux measurements.

We use the unprecedented spatial resolution of *Herschel* to derive resolved dust properties within our objects and study the robustness of our result with our SED model assumptions (emissivity index, SED coverage, resolution). Our study at local scale shows that:

(i) When we fix the cold emissivity index to a standard $\beta_c = 2.0$, we obtain a smooth distribution of the cold temperatures, with a radial decrease towards the outer parts of galaxies. In some objects, the temperature distribution follows the distribution of star-forming regions (NGC 3627, for instance). Fixing β_c to 1.5 or 1.0 influences the temperature range derived but does not strongly modify the temperature relative distribution.

(ii) When β_c is free, barred spirals (e.g. NGC 1097, 1316, 1512, 3351 or 3627) show temperature distributions that are similar to those obtained with a fixed β_c and homogeneous emissivity index values across the galaxies. For non-barred galaxies, β_c seems to decrease with radius. We nevertheless obtain homogeneous cold temperature distributions for those objects. The fact that these temperature maps do not seem to relate to any dust heating sources questions the use of a free β in those objects. Applying a β -free model to deduce an average emissivity index across the galaxy and derive the temperature map using this median value could help to avoid potential degeneracies between T and β in those objects.

(iii) Gathering our local results in a T_c - β_c diagram clearly leads to a correlation between the two parameters. This correlation could be linked with (a) a real emissivity variation of dust grains with temperature; (b) noise effects and uncertainties on flux measurements; and (c) temperature mixing along the line of sight.

(iv) The dust mass surface density usually peaks in the centre of galaxies but also seems to coincide with extranuclear peaks of star formation at the end of the bars (usually corresponding to molecular gas reservoirs).

(v) The dust mass estimates seem to be affected by resolution, with a systematic increase in total dust masses in the ‘resolved’ case compared to dust masses globally determined.

(vi) The submm coverage of our SEDs with *Herschel* observations modifies the dust masses compared to those derived from *Spitzer*-based fits. Two-MBB fits performed with data up to 250 μm differ from those derived using the complete SPIRE coverage (data up to 500 μm) by up to 17 per cent if $\beta_c = 2.0$ and up to 30 per cent if $\beta_c = 1.0$.

(vii) Dust masses derived globally or on a local basis using the DL07 model only differ from those derived from models using

MBBs and $\beta_c = 2.0$ by less than 30 per cent. Dust masses derived from MBB fits using a shallower parameter β_c are systematically lower than those derived with $\beta_c = 2.0$ (lower by 25–46 per cent if $\beta = 1.5$, for instance, in our sample). Our results highlight the necessity to better investigate the variations of the cold dust properties to properly quantify the total dust mass if we aim, for instance, to use it as a gas tracer.

This study aimed to investigate the properties of cold dust unveiled by *Herschel* observations of nearby galaxies. Questions remain due to possible degeneracies between the grain emissivities and temperatures. Moreover, this paper uses isothermal fits, which implies that the intrinsic emissivity index of the dust grains and the emissivity index directly obtained from our fits are one and the same. The presence of several dust grain temperatures in our objects both locally and at global scale also makes a direct extrapolation of dust properties difficult. Nevertheless, combining those results with other derived quantities such as the elemental abundances in the ISM or reliable gas-to-dust mass ratios as well as further investigations on closer objects will help us to disentangle between the different hypotheses.

ACKNOWLEDGMENTS

We would first like to thank the referee for his/her helpful comments which helped to improve the clarity of the paper. FST acknowledges support by the DFG via the grant TA 801/1-1. The research of CDW is supported by grants from the Natural Sciences and Engineering Research Council of Canada. PACS has been developed by MPE (Germany); UVIE (Austria); KU Leuven, CSL, IMEC (Belgium); CEA, LAM (France); MPIA (Germany); INAF-IFSI/OAA/OAP/OAT, LENS, SISSA (Italy); and IAC (Spain). This development has been supported by BMVIT (Austria), ESA-PRODEX (Belgium), CEA/CNES (France), DLR (Germany), ASI/INAF (Italy) and CICYT/MCYT (Spain). SPIRE has been developed by a consortium of institutes led by Cardiff University (UK) and including: University of Lethbridge (Canada); NAOC (China); CEA, LAM (France); IFSI, Padua University (Italy); IAC (Spain); Stockholm Observatory (Sweden); Imperial College London, RAL, UCL-MSSL, UKATC, University of Sussex (UK); and Caltech, JPL, NHSC, University of Colorado (USA). This development has been supported by national funding agencies: CSA (Canada); NAOC (China); CEA, CNES, CNRS (France); ASI (Italy); MCINN (Spain); SNSB (Sweden); STFC, UKSA (UK); and NASA (USA).

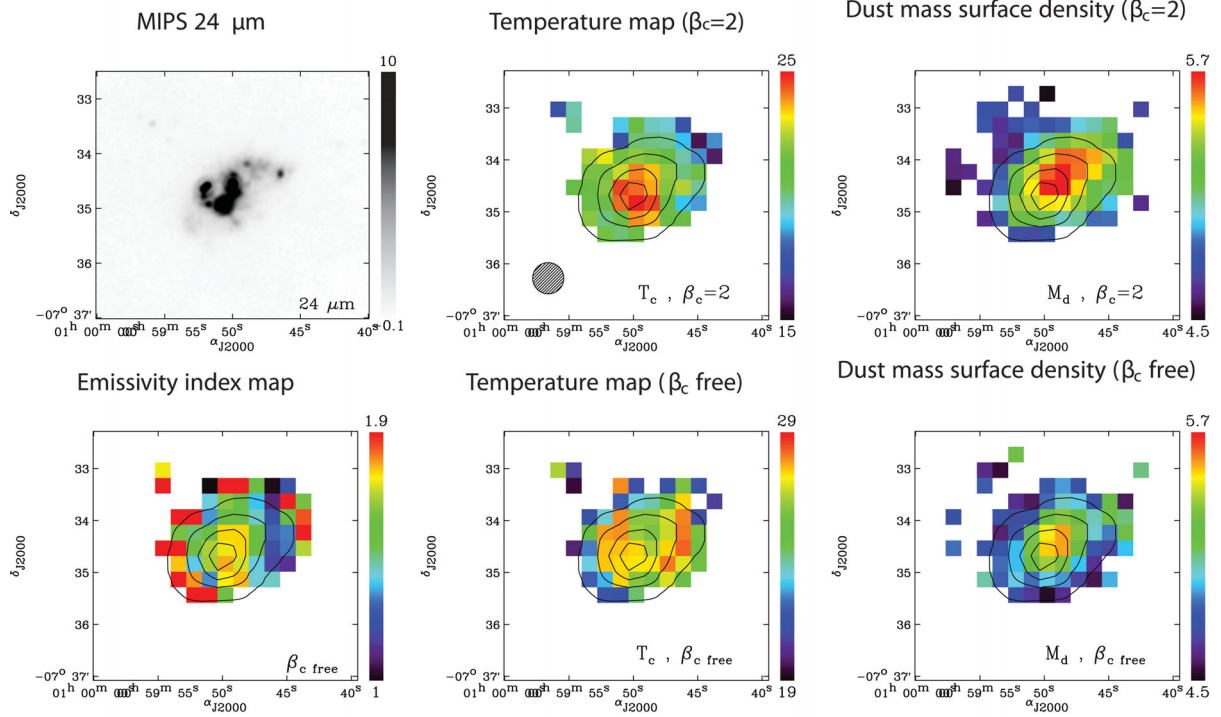
REFERENCES

- Abergel A. et al. (Planck Collaboration), 2011, *A&A*, 536, A25
 Ade P. A. R. et al. (Planck Collaboration), 2011a, *A&A*, 536, A16
 Ade P. A. R. et al. (Planck Collaboration), 2011b, *A&A*, 536, A17
 Aniano G., Draine B. T., Gordon K. D., Sandstrom K., 2011, *PASP*, 123, 1218
 Aniano G. et al., 2012, *ApJ*, in press (A12a)
 Auld R. et al., 2012, *MNRAS*, 420, 1882
 Beirão P. et al., 2010, *A&A*, 518, L60
 Bendo G. J. et al., 2003, *AJ*, 125, 2361
 Bendo G. J. et al., 2006, *ApJ*, 652, 283
 Bendo G. J. et al., 2012, *MNRAS*, 419, 1833
 Bernard J.-P. et al., 2008, *AJ*, 136, 919
 Boquien M. et al., 2011, *AJ*, 142, 111
 Boselli A. et al., 2010, *A&A*, 518, L61
 Bot C., Boulanger F., Lagache G., Cambréys L., Egret D., 2004, *A&A*, 423, 567

- Bot C. et al., 2010, *A&A*, 524, A52
- Boulanger F., Abergel A., Bernard J.-P., Burton W. B., Desert F.-X., Hartmann D., Lagache G., Puget J.-L., 1996, *A&A*, 312, 256
- Calzetti D., 2007, *Nuovo Cim. B*, 122, 971
- Calzetti D. et al., 2010, *ApJ*, 714, 1256
- Cazaux S., Caselli P., Tielens A. G. G. M., LeBourlot J., Walmsley M., 2005, *J. Phys. Conf. Ser.*, 6, 155
- Dale D. A. et al., 2005, *ApJ*, 633, 857
- Dale D. A. et al., 2007, *ApJ*, 655, 863
- Dale D. A. et al., 2012, *ApJ*, 745, 95 (D12)
- Dominik C., Dullemond C. P., 2008, *A&A*, 491, 663
- Dominik C., Tielens A. G. G. M., 1997, *ApJ*, 480, 647
- Draine B. T., Li A., 2007, *ApJ*, 657, 810 (DL07)
- Draine B. T. et al., 2007, *ApJ*, 663, 866
- Dumke M., Krause M., Wielebinski R., 2004, *A&A*, 414, 475
- Dunne L., Eales S. A., 2001, *MNRAS*, 327, 697
- Dunne L., Eales S., Edmunds M., Ivison R., Alexander P., Clements D. L., 2000, *MNRAS*, 315, 115
- Dupac X. et al., 2003, *A&A*, 404, L11
- Ekers R. D., Goss W. M., Wellington K. J., Bosma A., Smith R. M., Schweizer F., 1983, *A&A*, 127, 361
- Ellison S. L., Nair P., Patton D. R., Scudder J. M., Mendel J. T., Simard L., 2011, *MNRAS*, 416, 2182
- Engelbracht C. W. et al., 2010, *A&A*, 518, L56
- Foyle K. et al., 2012, *MNRAS*, 421, 2917
- Friedli D., Benz W., Kennicutt R., 1994, *ApJ*, 430, L105
- Galametz M. et al., 2009, *A&A*, 508, 645
- Galametz M. et al., 2010, *A&A*, 518, L55
- Galametz M., Madden S. C., Galliano F., Honny S., Bendo G. J., Sauvage M., 2011, *A&A*, 532, A56
- Galliano F., Madden S. C., Jones A. P., Wilson C. D., Bernard J.-P., Le Peintre F., 2003, *A&A*, 407, 159
- Galliano F., Madden S. C., Jones A. P., Wilson C. D., Bernard J.-P., 2005, *A&A*, 434, 867
- Galliano F. et al., 2011, *A&A*, 536, A88
- Gordon K. D., Engelbracht C. W., Rieke G. H., Misselt K. A., Smith J.-D. T., Kennicutt R. C., Jr, 2008, *ApJ*, 682, 336
- Gordon K. D. et al., 2010, *A&A*, 518, L89
- Griffin M. J. et al., 2010, *A&A*, 518, L3
- Hasegawa T. I., Herbst E., 1993, *MNRAS*, 261, 83
- Hildebrand R. H., 1983, *Q. J. R. Astron. Soc.*, 24, 267
- Hinz J. L. et al., 2012, *ApJ*, in press (arXiv:1207.2777)
- Hirashita H., Omukai K., 2009, *MNRAS*, 399, 1795
- Horellou C., Black J. H., van Gorkom J. H., Combes F., van der Hulst J. M., Charmandaris V., 2001, *A&A*, 376, 837
- Hummel E., van der Hulst J. M., Keel W. C., 1987, *A&A*, 172, 32
- Israel F., 2000, in Combes F., Pineau Des Forets G., eds, *Molecular Hydrogen in Space*, p. 293
- James A., Dunne L., Eales S., Edmunds M. G., 2002, *MNRAS*, 335, 753
- Jones A. P., Tielens A. G. G. M., Hollenbach D. J., McKee C. F., 1994, *ApJ*, 433, 797
- Jones A. P., Tielens A. G. G. M., Hollenbach D. J., 1996, *ApJ*, 469, 740
- Juvela M., Ysard N., 2012, *A&A*, 539, A71
- Kennicutt R. C., Jr, 1998, *ApJ*, 498, 541
- Kennicutt R. C., Jr, et al., 2003, *PASP*, 115, 928
- Kennicutt R. C. et al., 2011, *PASP*, 123, 1347
- Kim D.-W., Fabbiano G., 2003, *ApJ*, 586, 826
- Kobulnicky H. A., Kewley L. J., 2004, *ApJ*, 617, 240 (KK)
- Lanz L., Jones C., Forman W. R., Ashby M. L. N., Kraft R., Hickox R. C., 2010, *ApJ*, 721, 1702
- Leroy A., Bolatto A. D., Simon J. D., Blitz L., 2005, *ApJ*, 625, 763
- Leroy A. K. et al., 2009, *AJ*, 137, 4670
- Li A., Draine B. T., 2001, *ApJ*, 554, 778
- Magnelli B. et al., 2012, *A&A*, 539, A155
- Markwardt C. B., 2009, in Bohlender D. A., Durand D., Dowler P., eds, *ASP Conf. Ser. Vol. 411, Astronomical Data Analysis Software and Systems XVIII. Astron. Soc. Pac., San Francisco*, p. 251
- Marleau F. R. et al., 2006, *ApJ*, 646, 929
- Meixner M. et al., 2010, *A&A*, 518, L71
- Mennella V., Brucato J. R., Colangeli L., Palumbo P., Rotundi A., Bussolletti E., 1998, *ApJ*, 496, 1058
- Mentuch Cooper E. et al., 2012, *ApJ*, in press (arXiv:1206.2989)
- Mény C., Gromov V., Boudet N., Bernard J.-P., Paradis D., Nayral C., 2007, *A&A*, 468, 171
- Moustakas J., Kennicutt R. C., Jr, Tremonti C. A., Dale D. A., Smith J.-D. T., Calzetti D., 2010, *ApJS*, 190, 233
- O'Halloran B. et al., 2010, *A&A*, 518, L58
- Paradis D., Bernard J., Mény C., 2009, *A&A*, 506, 745
- Parkin T. J. et al., 2012, *MNRAS*, 422, 2291
- Pilbratt G. L. et al., 2010, *A&A*, 518, L1
- Pilyugin L. S., Thuan T. X., 2005, *ApJ*, 631, 231 (PT)
- Poglitsch A. et al., 2010, *A&A*, 518, L2
- Pohlen M. et al., 2010, *A&A*, 518, L72
- Roussel H., 2012, preprint (arXiv:1205.2576)
- Rowan-Robinson M. et al., 2010, *MNRAS*, 409, 2
- Sandstrom K. et al., 2010, *A&A*, 518, L59
- Serra Díaz-Cano L., Jones A. P., 2008, *A&A*, 492, 127
- Shetty R., Kauffmann J., Schnee S., Goodman A. A., Ercolano B., 2009, *ApJ*, 696, 2234
- Skibba R. A. et al., 2011, *ApJ*, 738, 89
- Smith M. W. L. et al., 2012, *ApJ*, in press (arXiv:1204.0785)
- Stepnik B. et al., 2003, *A&A*, 398, 551
- Stevens J. A., Amure M., Gear W. K., 2005, *MNRAS*, 357, 361
- Surace J. A., Sanders D. B., Mazzarella J. M., 2004, *AJ*, 127, 3235
- Tabatabaei F. S. et al., 2011, in Tuffs R. J., Popescu C. C., eds, *Proc. IAU Symp. 284, The Spectral Energy Distribution of Galaxies*. (arXiv:1111.6740)
- Taylor C. L., Kobulnicky H. A., Skillman E. D., 1998, *AJ*, 116, 2746
- van Driel W., Rots A. H., van Woerden H., 1988, *A&A*, 204, 39
- Vidali G., Roser J. E., Manicó G., Pirronello V., 2004, *J. Geophys. Res. (Planets)*, 109, 7
- Warren B. E. et al., 2010, *ApJ*, 714, 571
- Wilson C. D., 1995, *ApJ*, 448, L97
- Wolfire M. G., Hollenbach D., McKee C. F., 2010, *ApJ*, 716, 1191

APPENDIX A: DUST TEMPERATURE, EMISSIVITY INDEX AND DUST MASS SURFACE DENSITY MAPS

NGC 337



NGC 628

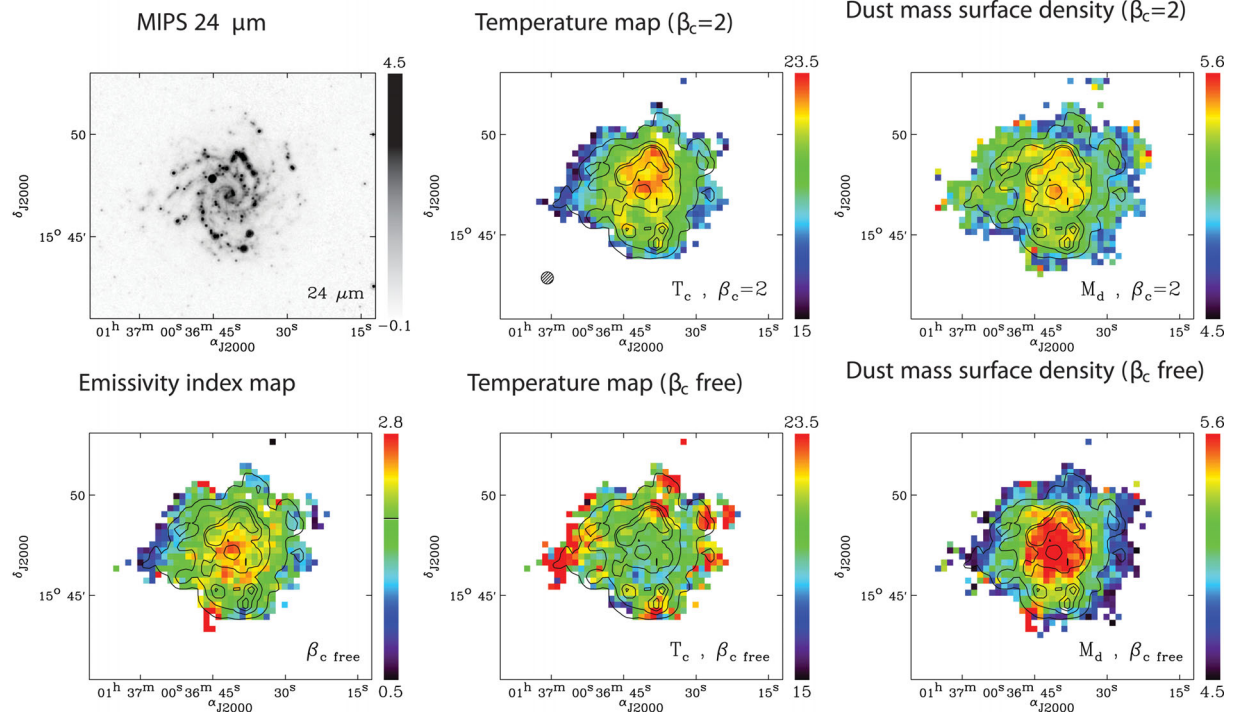
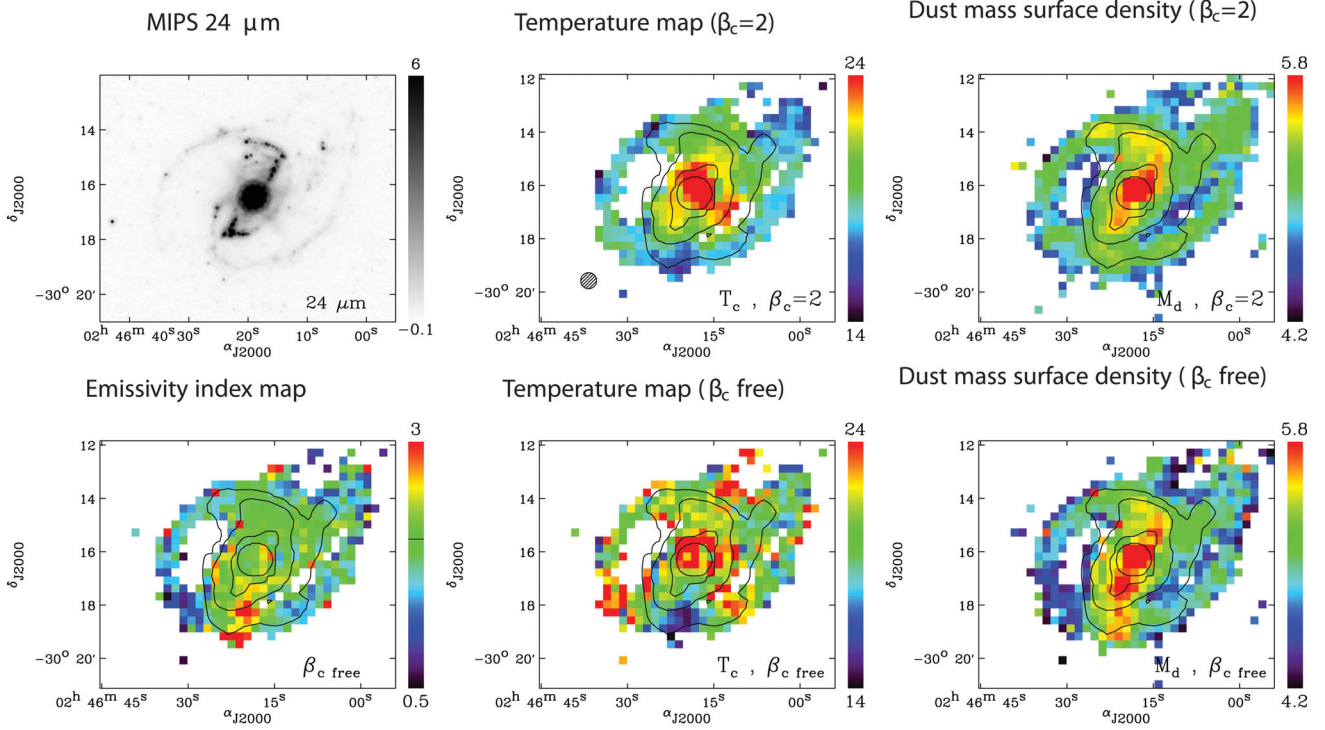


Figure A1. For each galaxy, north is up and east is left. Top part: MIPS 24 μm image (MJy sr^{-1}), cold dust temperature map (in K) and dust mass surface density map (in $M_{\odot} \text{kpc}^{-2}$, log scale) derived with $\beta_c = 2.0$. All images are convolved to the SPIRE 500 μm PSF before deriving the parameter maps. The FWHM of the PSF of SPIRE 500 μm is shown by the dashed circle in the top middle panel for each galaxy. Bottom part: emissivity index map, cold dust temperature map (in K) and dust mass surface density map (in $M_{\odot} \text{kpc}^{-2}$, log scale) derived with T_c and β_c as free parameters. The value $\beta_c = 2.0$ is indicated on the colour scale of the emissivity index map. We overlay the MIPS 24 μm contours (smoothed to the resolution of the T - β maps) for comparison.

NGC 1097



NGC 1291

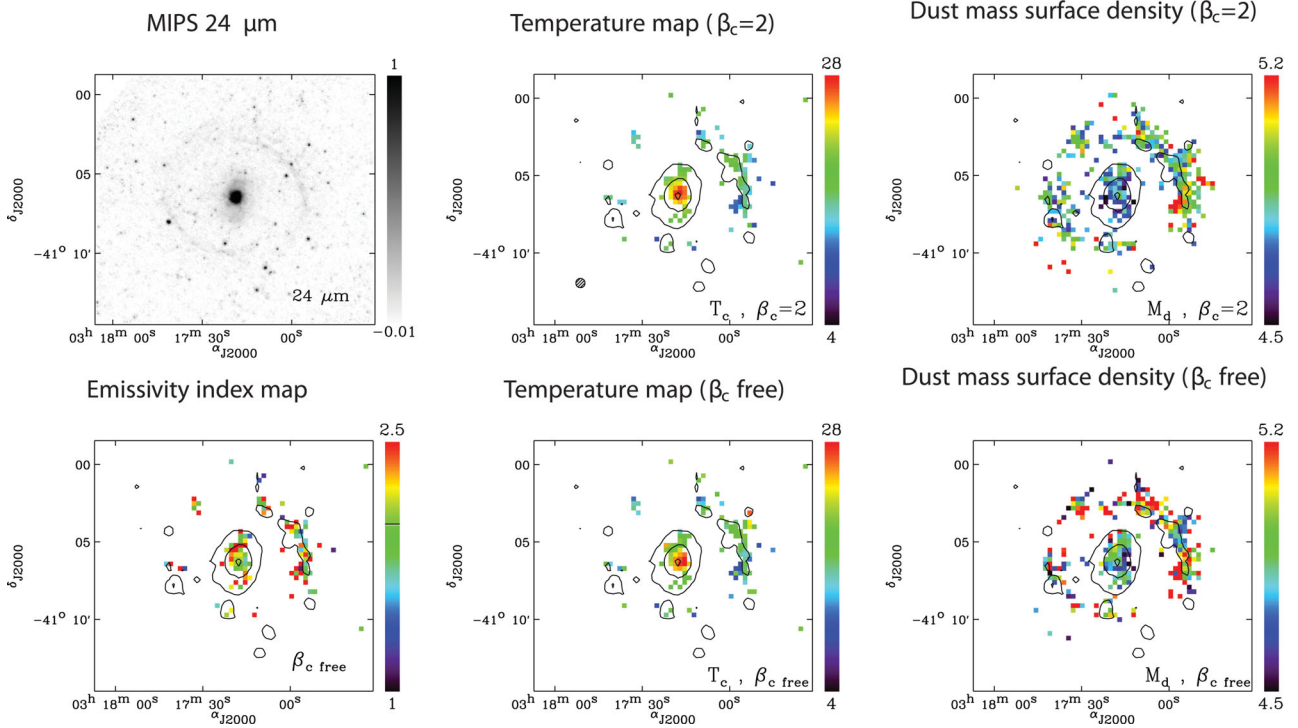
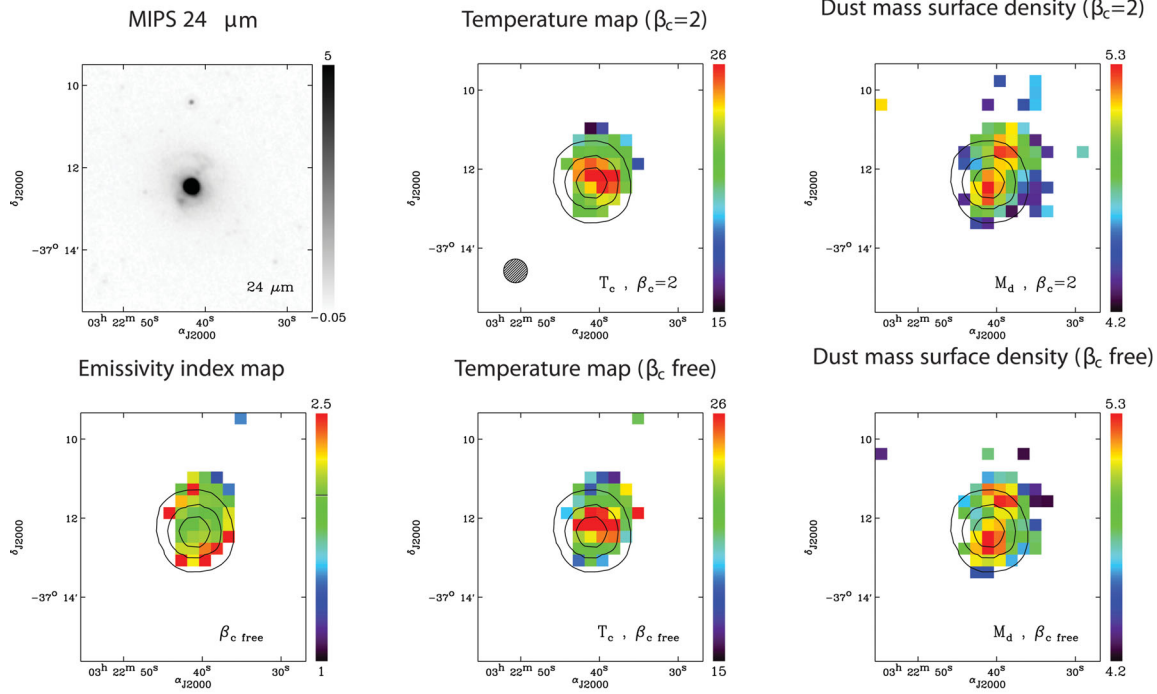
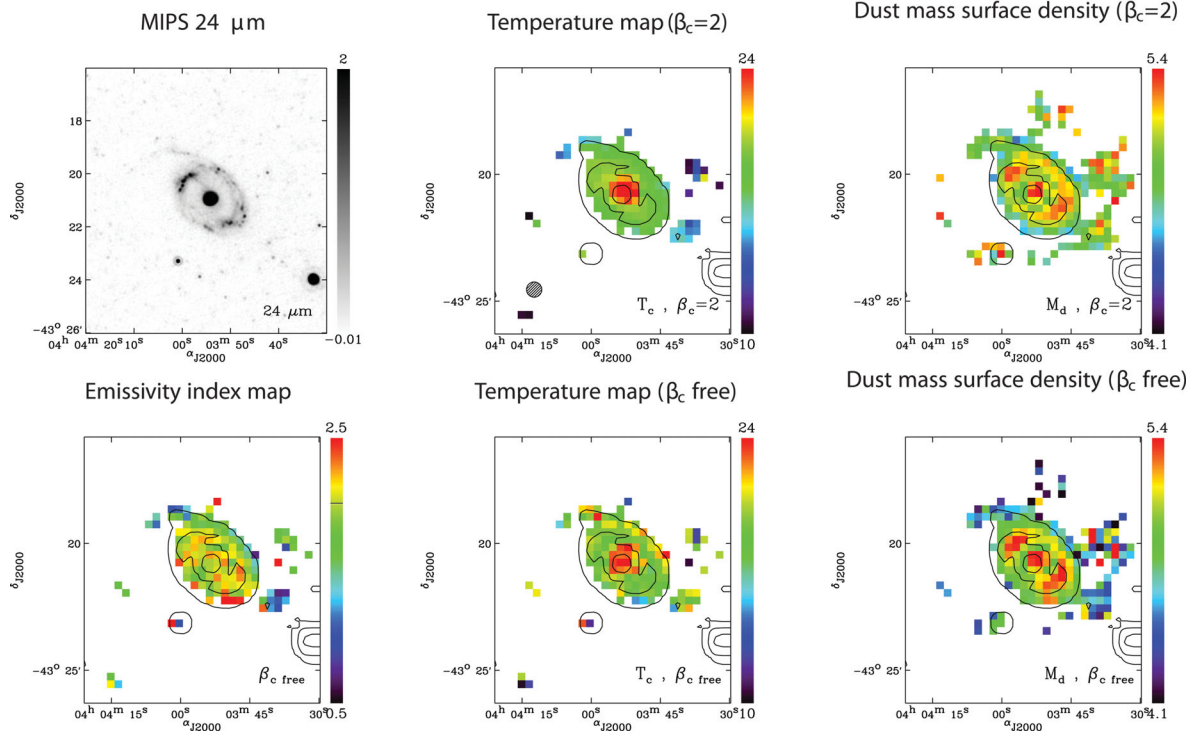


Figure A1 – continued

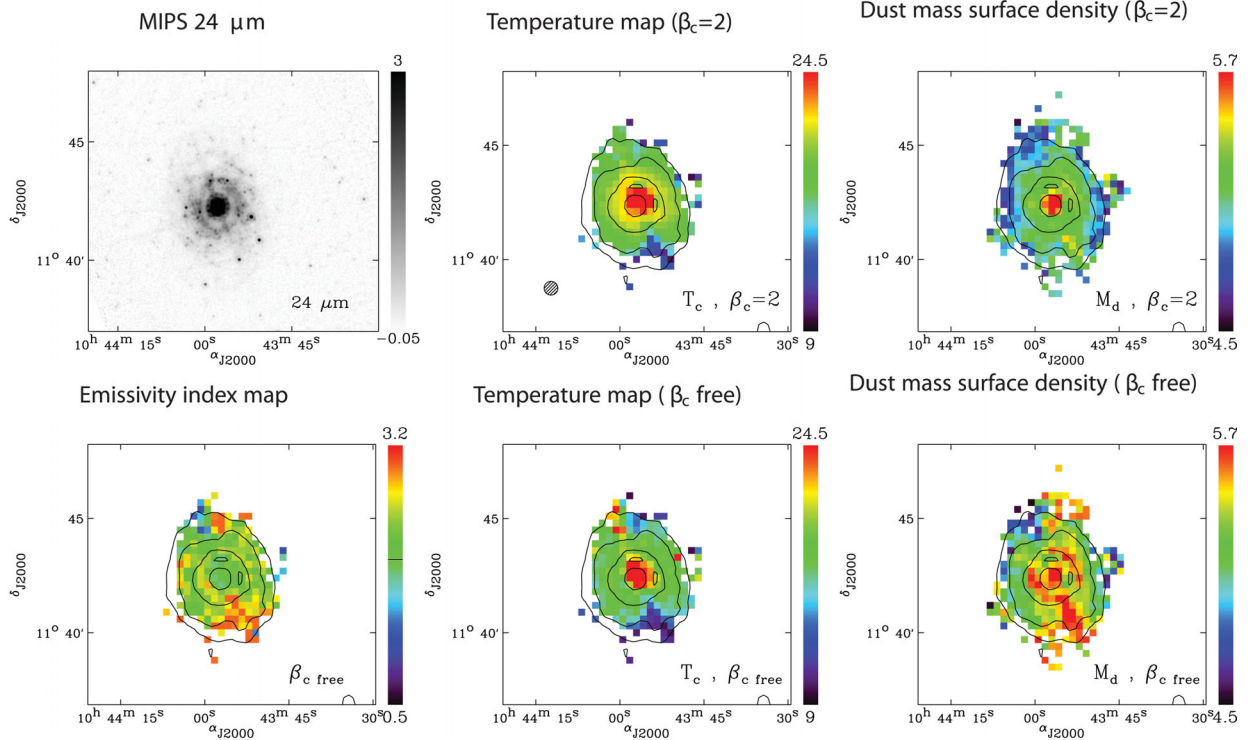
NGC 1316



NGC1512

Figure A1 – *continued*

NGC 3351



NGC 3621

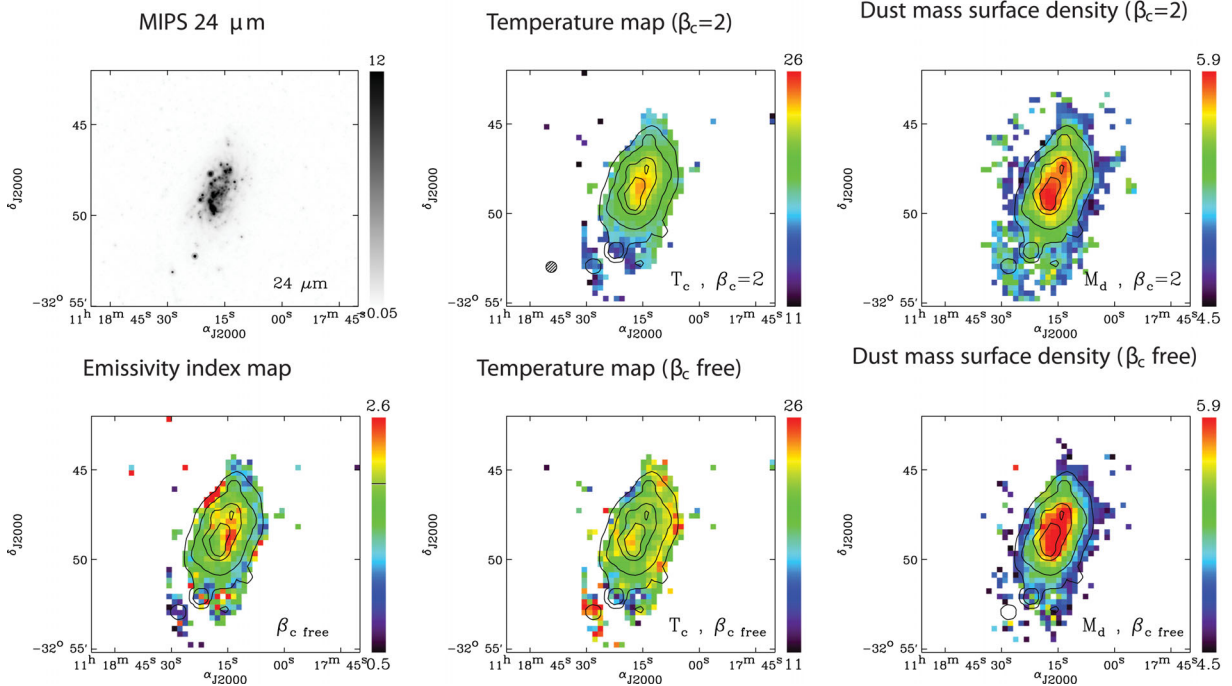
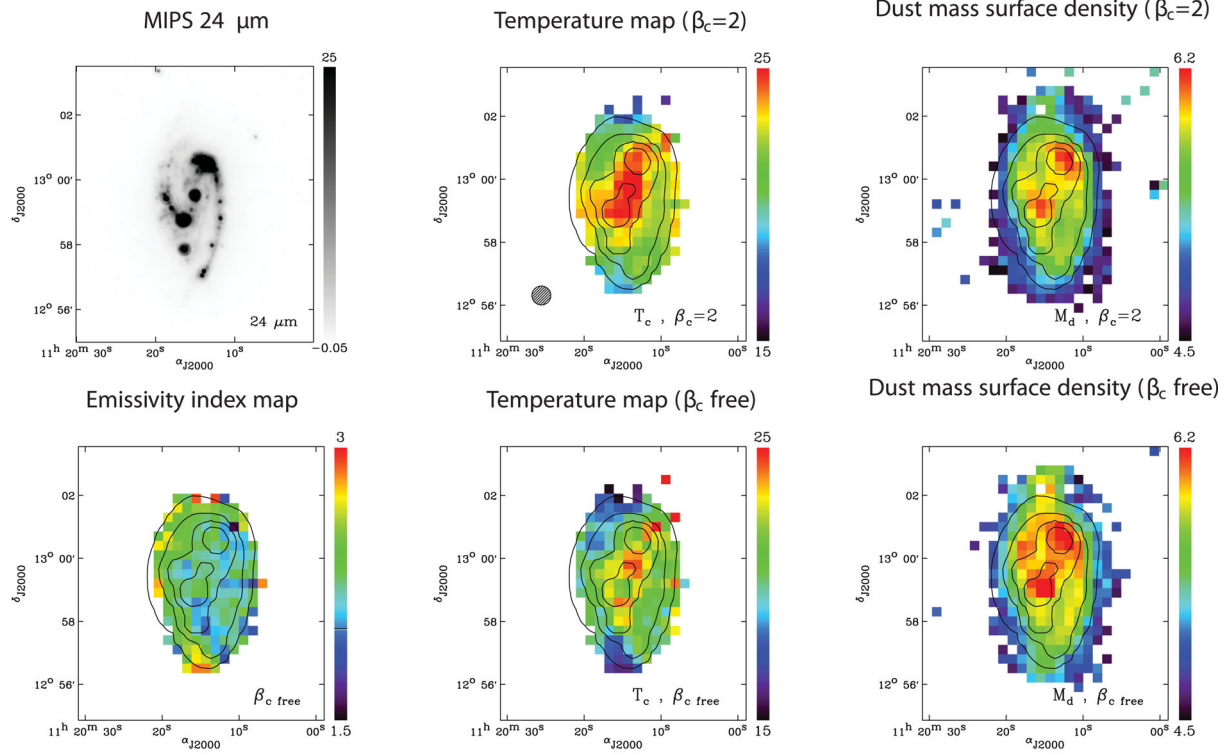


Figure A1 – continued

NGC 3627



NGC 4826

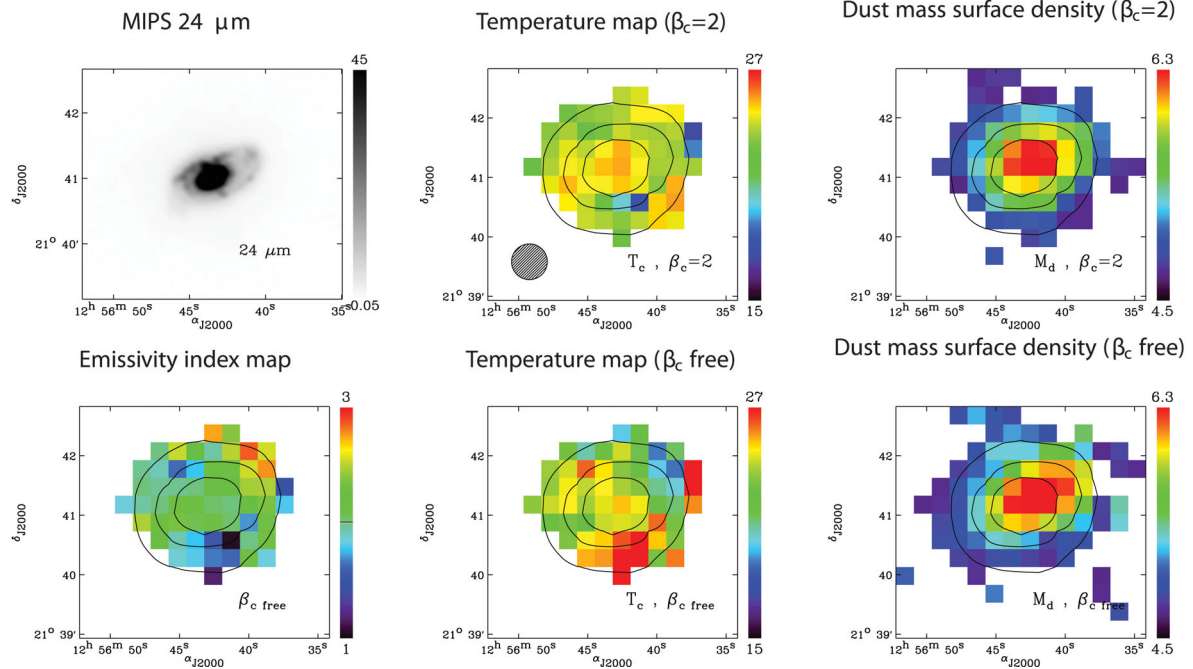


Figure A1 – continued

NGC 7793

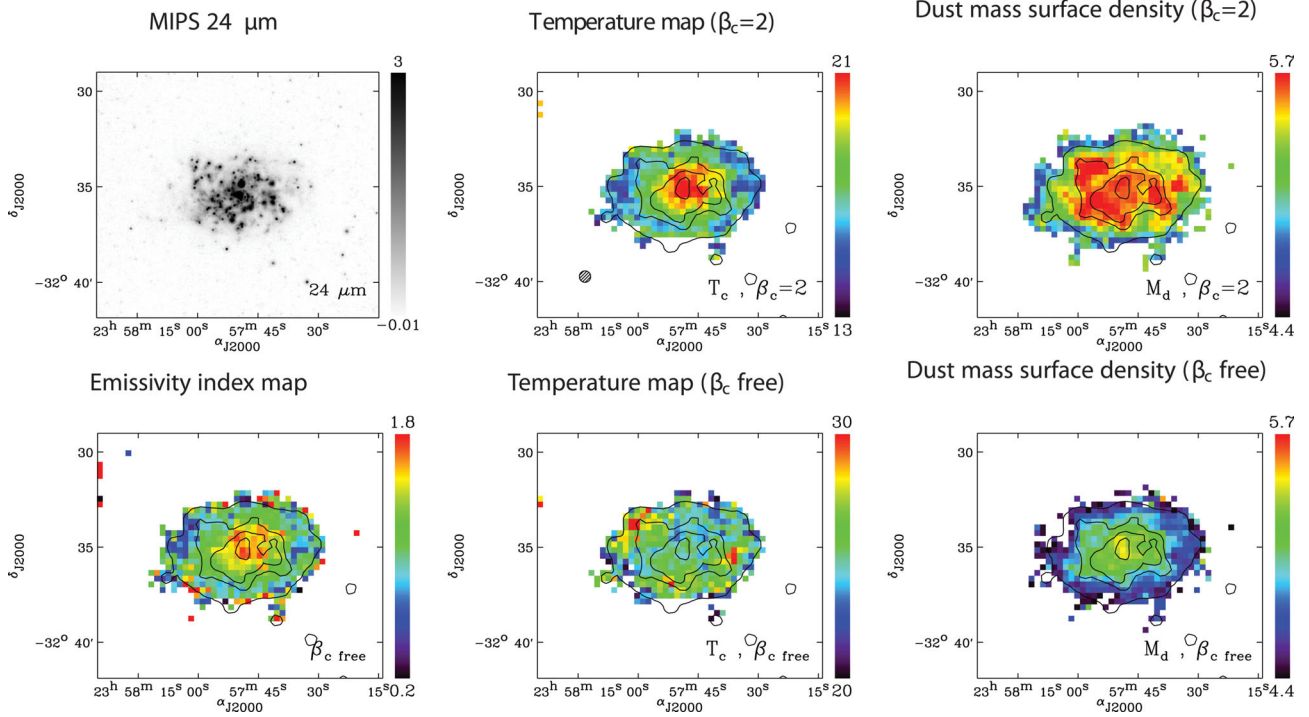


Figure A1 – continued

 This paper has been typeset from a $\text{\TeX}/\text{\LaTeX}$ file prepared by the author.